Journal of Computational Physics 279 (2014) 218–240

Contents lists available at ScienceDirect

Journal of Computational Physics

www.elsevier.com/locate/jcp

A robust absorbing layer method for anisotropic seismic wave modeling

L. Métivier [a,b,*], R. Brossier [b], S. Labbé [a], S. Operto [c], J. Virieux [b]

[a] LJK, CNRS, Université de Grenoble, BP 53, 38041 Grenoble Cedex 09, France
[b] ISTerre, Université de Grenoble I, BP 53, 38041 Grenoble Cedex 09, France
[c] Géoazur, Université de Nice Sophia-Antipolis, CNRS, IRD, OCA, Villefranche-sur-Mer, France

ARTICLE INFO

Article history:
Received 4 February 2014
Received in revised form 5 September 2014
Accepted 9 September 2014
Available online 18 September 2014

Keywords:
Seismic wave modeling
Hyperbolic problems
Absorbing layers
Perfectly matched layers
Anisotropy

ABSTRACT

When applied to wave propagation modeling in anisotropic media, Perfectly Matched Layers (PML) exhibit instabilities. Incoming waves are amplified instead of being absorbed. Overcoming this difficulty is crucial as in many seismic imaging applications, accounting accurately for the subsurface anisotropy is mandatory. In this study, we present the SMART layer method as an alternative to PML approach. This method is based on the decomposition of the wavefield into components propagating inward and outward the domain of interest. Only outgoing components are damped. We show that for elastic and acoustic wave propagation in Transverse Isotropic media, the SMART layer is unconditionally dissipative: no amplification of the wavefield is possible. The SMART layers are not perfectly matched, therefore less accurate than conventional PML. However, a reasonable increase of the layer size yields an accuracy similar to PML. Finally, we illustrate that the selective damping strategy on which is based the SMART method can prevent the generation of spurious *S*-waves by embedding the source in a small zone where only *S*-waves are damped.

1. Introduction

Accounting for the anisotropy of the subsurface in seismic wave propagation modeling is a crucial issue. At the exploration scale, in numerous environments, the subsurface does not satisfy the standard assumption of isotropic propagation. In sedimentary basins, for instance, the piling-up of small shale layers induce differences between horizontal and vertical wave velocities. Anisotropy is also observed near foothills environments, or in overthrust areas. With the current development of wide azimuth seismic acquisition systems, modern seismic imaging methods require robust modeling engines accounting accurately for the true Earth anisotropy. Indeed, these method rely on an accurate interpretation of the wave propagation, both in terms of kinematics and amplitude variations, two factors on which anisotropy can have a strong imprint.

The most natural way for accounting for anisotropy is to use an elastic description of the subsurface. In this case, the different types of anisotropy result in different expressions of the stiffness tensor which relates stress to strain components. The simplest types of anisotropy usually employed are Vertical Transverse Isotropy (VTI) or Horizontal Transverse Isotropy (HTI). In these two cases, the anisotropy symmetry axis is aligned with the vertical (VTI) or horizontal (HTI) axis. This

* Corresponding author.
E-mail address: ludovic.metivier@ujf-grenoble.fr (L. Métivier).
URL: http://www-ljk.imag.fr/membres/Ludovic.Metivier/ (L. Métivier).

http://dx.doi.org/10.1016/j.jcp.2014.09.007
0021-9991/

approximation is generalized to Tilted Transverse Isotropy (TTI) through the introduction of a tilt angle from the vertical axis defining the symmetry axis along with the anisotropy is aligned. More generic anisotropy description can also be considered: orthorombic anisotropy, or full (triclinic) anisotropy. In this latter case, the stiffness tensor associated with the 3D elastic dynamics is constituted of 21 independent parameters. In this study we will restrict to the simpler cases of VTI, HTI and TTI anisotropy. This three cases are also more generally referred to as Transverse Isotropy (TI).

The choice of an elastic wave propagation model may not be appropriate. First, in a modeling perspective, it is often difficult to obtain accurate estimation of parameters associated with the propagation of shear waves. Second, the computational cost associated with the solution of the corresponding system of equation is high. This is especially disadvantaging for seismic imaging methods such as Full Waveform Inversion [44] or Reverse Time Migration [22], which requires an important number of wave propagation problems to be solved at each step of the inversion. From the will to alleviate this computational burden originates the idea of designing acoustic anisotropic models [4]. Although these anisotropic acoustic models have no physical reality, the objective is to correctly describe the propagation of pressure waves (P-waves), while neglecting the propagation of shear waves (S-waves), under the assumption of weak-to-moderate anisotropy which characterizes geological media [42]. This approximation is also motivated by the observation that in numerous seismic exploration case studies, particularly in marine environment, the imprint of S-waves in the signal is weak and P-waves are dominant.

In practice, the acoustic anisotropic approximation is obtained by setting to 0 the S-wave velocity along the anisotropy symmetry axis, either from the dispersion relation associated with the linear elasticity equations, as initially proposed by Alkhalifah [3,4], and later on Zhou et al. [48], Operto et al. [38], or starting from an elastic description of the wave propagation, as promoted by Duveneck and Bakker [19].

Note that in general, the acoustic TI equations still include artificial S-wave modes. Indeed, even if the S-wave velocity is equal to zero along the anisotropy symmetry axis and directions perpendicular to this axis, its value may be non-zero in arbitrary directions [24]. For these equations, ad-hoc strategies have thus been designed to mitigate as much as possible the generation of spurious S-waves. We will see that the SMART layer method yields a complementary and efficient approach to overcome this difficulty.

For most of seismic modeling and imaging applications, the subsurface is considered as a semi-infinite medium. A free surface condition on top delineates the interface between the ground (or sea) and the air; the Earth is considered to extend infinitely in depth and lateral directions. However, the numerical domain in which the computation is performed is finite. It is therefore necessary to use Absorbing Boundary Conditions (ABC) or absorbing layers to avoid fictitious reflections.

First-order ABC (known also as radiation boundary conditions), introduced in the pioneering studies of Clayton and Engquist [14] and Engquist and Majda [21] are easy to implement for simple wave equations models, such as the acoustic wave equation. While these equations are exact in a mono-dimensional context (the outgoing waves are absorbed without introducing spurious reflections), this is not true for multi-dimensional problems. In particular, waves arriving to the boundary with grazing incidence generate spurious reflections. An improvement of these ABC can be achieved through the design of higher-order version [15,23]. If the accuracy of these ABC is improved, their implementation is more complex, as they imply the use of fractional high-order derivatives. In this case, the approximation of the differential operator at the boundary yields a complex system of equations to solve. In practice, it is difficult to guarantee the stability of such methods, and a correct absorption of waves at all incidence angles.

An alternative to absorbing boundary conditions consists in the design of absorbing layers: the domain of interest is surrounded with a layer where waves incoming from the domain of interest are artificially damped. This idea has first been promoted by Cerjan et al. [13] for the second-order in time acoustic equation. Despite this simple formalism, in practice, the design of such absorbing layer is difficult. Except for the 1D problem, the introduction of the layer generates reflections at the interface between the domain of interest and the layer. These reflections can be mitigated by choosing variable damping coefficient that smoothly grow from zero at the interface between the layer and the domain of interest, to the external boundary of the layer. However, this reduces the absorbing capability of the layer and requires to increase its size, which, in turn, increases the overall computational time of the simulation.

The Perfectly Matched Layers (PML) method, introduced by Bérenger [9], has become rapidly popular as it achieves an excellent trade-off between these two contradictory requirements. The initial method is based on a splitting of the hyperbolic system and the introduction of smooth damping coefficients in the layer. The PML strategy was originally designed for the 2D and 3D Maxwell's equation [9,10]. For these equations, a plane wave analysis demonstrates that the reflection coefficient at the interface between the domain of interest and the layer is null for wave propagating at all angles. In practice, the reflectivity for the discrete problem is not exactly zero, and when PML are used in heterogeneous models, a WKB analysis shows that only the leading order of the reflection coefficient is zero (see the review paper by Halpern et al. [25]). However, in many practical applications the amplitude of the spurious reflected waves remains very small.

Because of this remarkable property, the PML method is now the standard for the simulation of wave propagation in numerous applications. The method has been progressively extended to different wave propagation systems, from acoustic wave propagation, [39,17,11], to linearized Euler equations [28,27,2], and linear elasticity [26,16,6,31,5]. Later on, Convolutional PML (C-PML) [30,34,33] have been proposed to improve the absorption of wave propagating at grazing angles to the interface between the domain of interest and the layer. This method is based on a generalization of the complex-valued stretching related to the standard PML formulation in the frequency-domain.

However, when applied to the modeling of wave propagation in anisotropic media, the PML and C-PML methods become amplifying, which causes difficulties for their application to this particular case. This amplification has first been noted in

the case of 2D linear elasticity for VTI media by Becache et al. [7], and later on in the case of 2D acoustic TTI equations [38,19,47]. The modification of the PML through the C-PML technique does not prevent from this amplification phenomena [30].

The amplification analysis proposed by Becache et al. [7] is based on slowness diagrams. In particular, they show that when the slowness vector and the group velocity are in opposite directions, the PML becomes amplifying. This amplification phenomenon, numerically experimented in the aforementioned studies, has also been formalized through a WKB analysis by Halpern et al. [25]. Depending on the symbol of the propagation operator associated with the PML strategy, one can see that the amplification phenomenon is actually common. Acoustic and electromagnetic wave equations are particular cases for which the amplification does not occur, but this is not true in general.

These analysis suggest that the use of PML and C-PML for the simulation of wave propagation in anisotropic media is not the appropriate choice, raising again the question of a suitable choice of absorbing conditions. Recent works have been devoted to the design of new high-order ABC for the propagation of waves in anisotropic media [45,8]. A generalization of the standard PML scheme has also been proposed under the name of Modified PML (M-PML) by Meza-Fajardo and Papageorgiou [37]. Whereas for standard PML, the damping coefficients introduced in the layer vary only in the direction normal to the interface between the domain of interest and the layer, the M-PML strategy introduces additional absorption terms in the directions tangential to this interface. The introduction of this tangential damping can be actually interpreted as a trade-off between a standard PML (no tangential absorption) and a standard sponge layer (same level of tangential and normal absorption) [13]. The M-PML is thus not perfectly matched [18]. In their study, Meza-Fajardo and Papageorgiou [37] show that a sufficient level of tangential anisotropy may prevent the amplification phenomenon. However, it is difficult to correctly define this level as this task is intrinsically problem dependent. Besides, the required amplitude may be large, making the layer method close from a sponge layer, which may yield high amplitude spurious reflections.

In this study we investigate how another absorbing layer method, named SMART layers [25], can be applied to the acoustic anisotropic equations. The SMART layer is a generalization of a layer method initially introduced by Israeli and Orszag [29] as an approximation of radiation boundary conditions. A diagonalization of the matrices which compose the leading symbol of the first-order hyperbolic operator yields a natural decomposition of the solution into components propagating inward and outward the domain of interest in each spatial direction. This decomposition is used to select the components to be damped, depending on the position in the computational domain. In the domain of interest, no damping is applied. In the left layer, only components of the solution propagating leftward are damped, and similarly for the other layer sides. The decomposition is applied at the continuous level, and results in the introduction of a zero-order term into the PDE.

For hyperbolic systems satisfying a symmetrizability condition, this zero-order term is dissipative: this is demonstrated in Section 2. This property guarantees that the SMART layer method does not generate artificial amplification, contrary to PML, in the anisotropic case.

The symmetrizability condition requires the existence of a symmetrizer common to all the matrices which compose the leading-order symbol of the first-order differential operator. In Section 3, we show that the VTI elastic system satisfies this symmetrizability condition, as well as the acoustic VTI and TTI equations derived from this system following the approach of Duveneck and Bakker [19]. The symmetrizer is explicitly built from the compliance matrix (the inverse of the stiffness tensor) which relates the stress tensor to the strain tensor.

As only the introduction of a zero-order term is involved in their design, the SMART layers could be related to the sponge layer strategy. In the framework of sponge layers, the dissipative zero-order term which is introduced is simply the identity operator. We begin Section 4 with a numerical comparison which illustrates that the reflectivity of the SMART layers is improved with respect to the sponge layer method. The comparison with PML also illustrates that the reflectivity of the SMART layers at the interface between the computational domain and the layer is larger. Thus, in a non-amplifying regime, for equivalent layer size, the PML method remains more accurate. However we show that the accuracy of the PML method can be reached at the expense of a reasonable increase of the SMART layer width. The computational cost associated to this increase may however be compensated by the fact that the SMART layer only requires the introduction of a zero-order term in the original equation, while the PML method requires additional fields or memory variables.

This experiment is followed by a numerical comparison between SMART layers and PML for the acoustic TTI equations, in the case of anelliptical anisotropy. This experiment exhibits the amplifying behavior of PML in this context. We emphasize the robustness of the SMART layer method: no amplification is observed using SMART layers, contrary to PML approach.

Finally, another interesting property of the SMART layer strategy is illustrated in Section 4. For the acoustic TI equation, spurious S-wave may be generated. The selective damping strategy on which relies the SMART method provides a simple remedy to this problem: the source can be embedded into a Gaussian zone in which S-waves are strongly damped. Numerical results demonstrate that this strategy efficiently reduces the generation of spurious S-waves, even using a small size damping zone. Conclusion and perspectives are given in Section 5.

2. Analysis of the SMART layer strategy

2.1. A didactic example: the 1D acoustic wave equation

Consider the first-order acoustic wave equation in a homogeneous medium

$$\begin{cases} \partial_t u_z = \dfrac{1}{\rho_0}\partial_z p \\ \partial_t p = \rho_0 c_0^2 \partial_z u_z + s_p, \end{cases} \tag{1}$$

where $u_z(z,t)$ is the vertical velocity displacement, $p(z,t)$ is the pressure wavefield, c_0 is the constant pressure wave velocity, ρ_0 is the constant density and $s_p(z,t)$ is an explosive source term (Dirac function in space). The system (1) can be rewritten compactly in the form of a hyperbolic system

$$\partial_t u + A\partial_z u = s, \tag{2}$$

where

$$u = [u_z \quad p]^T, \qquad s = [0 \quad s_p]^T, \qquad A = -\begin{pmatrix} 0 & \frac{1}{\rho_0} \\ \rho_0 c_0^2 & 0 \end{pmatrix}. \tag{3}$$

The matrix A is diagonalizable. Its eigenvalues are c_0 and $-c_0$. We denote $(u^+, u^-) \in \mathbb{R}^2 \times \mathbb{R}^2$ the corresponding eigenvectors, and $P \in \mathbb{M}_2(\mathbb{R})$ the change of coordinates matrix such that $P^T = [u^+ \; u^-]$. We define $v(z,t)$ such that $v(z,t) = Pu(z,t)$, solution of

$$\begin{cases} \partial_t v_1 = c_0 \partial_z v_1 + (Ps)_1 \\ \partial_t v_2 = -c_0 \partial_z v_2 + (Ps)_2. \end{cases} \tag{4}$$

The system (4) consists in the superposition of the propagation of two plane waves: $v_1(z,t)$ propagates downward, while $v_2(z,t)$ propagates upward. Absorbing outgoing downward and upward propagating waves becomes easy: this can be performed through the introduction of a damping term $d^+(z)v_1(z,t)$ in the first equation of system (4) (respectively $d^-(z)v_2(z,t)$ in the second equation of system (4)). The coefficients $d^+(z)$ and $d^-(z)$ are zero in the domain of interest and grow smoothly in absorbing layers defined at the top and the bottom of the 1D domain.

Defining the matrices

$$E^+ = \begin{pmatrix} 1 & 0 \\ 0 & 0 \end{pmatrix}, \qquad E^- = \begin{pmatrix} 0 & 0 \\ 0 & 1 \end{pmatrix}, \tag{5}$$

the introduction of the absorbing layer thus amounts to the introduction of the zero-order terms $d^+(z)P^T E^+ Pu(z,t)$ and $d^-(z)P^T E^- Pu(z,t)$ in the initial system (2)

$$\partial_t u + A\partial_z u + d(z)^+ P^T E^+ Pu + d(z)^- P^T E^- Pu = s. \tag{6}$$

As mentioned in [29,9,25], these absorbing layers are perfectly matched: the reflection coefficient at the interface between the layer and the domain of interest is zero. The choice of a layer width of approximately one wavelength of the dominant signal is sufficient to provide a satisfactory decrease of the waves in the layer [29]. The extension to a multi-dimensional framework of this selective damping strategy yields the SMART layer method [25].

2.2. Multi-dimensional extension

Consider the general first-order hyperbolic system

$$\begin{cases} \partial_t u + \displaystyle\sum_{j=1}^{d} A_j(x)\partial_j u + A_0(x)u = f(x,t), \quad (x,t) \in \mathbb{R}^d \times [0,T], \; d \in \mathbb{N}, \\ u(x,0) = u_0(x), \end{cases} \tag{7}$$

where d is the dimension and

$$\begin{cases} u(x,t) \in L^2\big(\Omega \times [0,T], \mathbb{R}^p\big), \qquad f(x,t) \in L^2\big(\Omega \times [0,T], \mathbb{R}^p\big), \qquad u_0(x) \in L^2\big(\Omega, \mathbb{R}^p\big), \\ \forall x \in \mathbb{R}^d, \quad A_j(x) \in \mathbb{M}_p(\mathbb{R}). \end{cases} \tag{8}$$

The key point to define the SMART layer method is to identify the operators $P^T E^+ P$ and $P^T E^- P$ defined in the previous section as the spectral projectors on the eigenspaces $\ker(A - cI)$ and $\ker(A + cI)$. Provided the matrices $A_j(x)$, $j \geq 1$ are diagonalizable with real eigenvalues, the SMART layer method can be adapted to the multi-dimensional case through the definition of spectral projections on the eigenspaces of these matrices. For each matrix $A_j(x)$, $j \geq 1$, the solution of the system (7) can be decomposed in the basis formed by its eigenvectors. Components of the solution associated with positive eigenvalues (respectively with negative eigenvalues) of the matrix $A_j(x)$, $j \geq 1$ propagate in the direction $x_j > 0$ (respectively in the direction $x_j < 0$). The SMART layer system derived from the system (7) can thus be written as

$$\begin{cases} \partial_t u + \displaystyle\sum_{j=1}^{d} A_j(x)\partial_j u + A_0(x)u + B(x)u = f(x,t), \quad (x,t) \in \Omega \times [0,T], \; \Omega \subset \mathbb{R}^d, \; d \in \mathbb{N}, \\ u(y,t) = g(y,t), \quad (y,t) \in \partial\Omega \times [0,T], \\ u(x,0) = u_0(x), \end{cases} \tag{9}$$

where Ω is the bounded computational domain, $g(y,t)$ the boundary condition imposed on $\partial\Omega$, and the additional zero-order term $B(x)$ is a linear combination of spectral projections on the eigenspaces associated with positive and negative eigenvalues of the operators $A_j(x)$, $j \geq 1$. Defining the computational domain Ω as

$$\Omega = \prod_{j=1}^{d} [a_j - L_j, b_j + L_j], \quad L_j \in \mathbb{R}, \tag{10}$$

and the domain of interest as $\mathring{\Omega}$ as

$$\mathring{\Omega} = \prod_{j=1}^{d} [a_j, b_j], \tag{11}$$

we may introduce the coefficients $d_j^{\pm}(x_j)$ as smooth mono-dimensional functions which are zero in $\mathring{\Omega}$ and have a polynomial growth in the layer $\Omega \backslash \mathring{\Omega}$

$$\begin{cases} \forall x \in [a_j - L_j, b_j], \quad d_j^+(x_j) = 0, \qquad \forall x \in [b_j, b_j + L_j], \quad d_j^+(x_j) > 0 \\ \forall x \in [a_j, b_j + L_j], \quad d_j^-(x_j) = 0, \qquad \forall x \in [a_j - L_j, a_j], \quad d_j^-(x_j) > 0. \end{cases} \tag{12}$$

We may thus define $B(x)$ as

$$B(x) = \sum_{j=1}^{d} \sum_{n=1}^{n_j^+} d_j^+(x_j) B_{j,n}^+(x) + \sum_{j=1}^{d} \sum_{n=1}^{n_j^-} d_j^-(x_j) B_{j,n}^-(x), \tag{13}$$

where n_j^+ (respectively n_j^-) denotes the number of positive (respectively negative) eigenvalues of the matrix $A_j(x)$ and $B_{j,n}^+(x)$ (respectively $B_{j,n}^-(x)$) denotes the spectral projector on the corresponding eigenspace. The coefficients $d_j^{\pm}$ ensure that no attenuation is introduced in the domain of interest $\mathring{\Omega}$, as $B(x)$ is zero in $\mathring{\Omega}$.

Note that the standard sponge layer technique amounts to defining $B(x)$ as

$$B(x) = \sum_j d_j^{\pm}(x_j) I = \alpha(x) I, \tag{14}$$

with

$$\alpha(x) = \sum_j d_j^{\pm}(x_j). \tag{15}$$

2.3. Robustness of SMART layers

We first introduce the following definitions.

Definition 1. The system (7) is symmetrizable if and only if there exists a symmetrizer $S(x) \in \mathbb{M}_p(\mathbb{R})$ such that

$$\forall x \in \Omega, \quad S^T(x) = S(x), \qquad S(x) > 0, \qquad \big(S(x)A_j(x)\big)^T = S(x)A_j(x), \quad 1 \leq j \leq d. \tag{16}$$

Note that a symmetrizable system is strongly hyperbolic in the sense of Kreiss and Lorenz [32]. Thus it is strongly well-posed, and the L^2 norm of the solution at time t is controlled by the L^2 norm of the solution at $t = 0$. Conversely, a hyperbolic problem may be strongly hyperbolic but not symmetrizable.

Definition 2. The S-norm $\|.\|_S$ associated with a symmetric definite matrix $S(x) \in \mathbb{M}_p(\mathbb{R})$ is such that

$$\big\|u(.,t)\big\|_S = (Su,u)_{L^2} = \int_{\Omega} \big\langle S(x)u(x,t), u(x,t)\big\rangle dx, \tag{17}$$

where $\langle .,. \rangle$ denotes the Euclidean scalar product of $\mathbb{R}^p$.

With these definitions at hand, we can prove the following theorem.

Theorem 1. *Assume that*

- *the system (7) is symmetrizable with a symmetrizer $S(x)$;*
- *the coefficient of the matrices $S(x)A_j(x)$ belong to $\mathbb{W}^{1,\infty}$ (regularity condition).*

Then we can prove that

- *the SMART layer strategy can be applied to the system (7): the matrices $A_j(x)$ are diagonalizable with real eigenvalues;*
- *the zero-order term $B(x)$ added by the SMART layer method is dissipative: this ensures that no spurious amplification will be introduced.*

In particular, we have

$$\frac{d}{dt}\big\|u(.,t)\big\|_S^2 \leq (\gamma+1)\big\|u(.,t)\big\|_S^2 + \big\|f(.,t)\big\|_S^2 - 2(SBu,u)_{L^2}, \tag{18}$$

where

$$\gamma = \sum_{j=1}^{d} \sup_x \big|\partial_x(SA_j)\big| + \sup_x \big|(SA_0)\big|. \tag{19}$$

The inequality $(SBu,u)_{L^2} \geq 0$ ensures that the SMART zero-order term does not generate any energy growth. No amplification can be caused by its introduction as it is a dissipative term.

Proof. We first prove the applicability of the SMART method to hyperbolic symmetrizable systems. We have seen in the previous section that the SMART layers may apply to systems of the form (7) for which the matrices $A_j(x)$ are diagonalizable with real eigenvalues. We first prove that this is the case for symmetrizable systems. According to the definition there exists a symmetric positive definite operator $S(x)$ such that, $S(x)A_j(x)$ is real symmetric. We can define its square root $S(x)^{1/2}$ (also symmetric definite positive). The matrix

$$M(x) = S(x)^{1/2}A_j(x)S(x)^{-1/2}, \tag{20}$$

is real symmetric. Therefore $M(x)$ is diagonalizable, and there exists an orthogonal matrix $P(x)$ and a diagonal real matrix $D(x)$ such that

$$M(x) = P(x)D(x)P^T(x). \tag{21}$$

Then, we can rewrite $A_j(x)$ as

$$A_j(x) = S(x)^{-1/2}P(x)D(x)P(x)^T S(x)^{1/2} = Q(x)D(x)Q(x)^{-1}, \tag{22}$$

where

$$Q(x) = S(x)^{-1/2}P(x). \tag{23}$$

Hence, the matrix $A_j(x)$ is similar to a real diagonal matrix.

We now prove the second property. For the sake of clarity, we will assume homogeneous Dirichlet boundary conditions at the external boundary

$$g(y,t) = 0, \quad (y,t) \in \partial\Omega \times [0,T]. \tag{24}$$

This is the condition which is used in practice. Choosing more general boundary conditions is possible, as it only generates additional boundary terms in the integration by parts. For $u(x,t)$ solution of (9), we have

$$\begin{aligned}\frac{d}{dt}\big\|u(.,t)\big\|_S^2 &= (S\partial_t u,u)_{L^2} + (Su,\partial_t u)_{L^2}\\ &= -\sum_{j=1}^{d}(SA_j\partial_x u,u)_{L^2} - \sum_{j=1}^{d}(Su,A_j\partial_x u)_{L^2} + 2(Su,f)_{L^2}\\ &\quad - 2(SA_0u,u)_{L^2} - 2(SBu,u)_{L^2}.\end{aligned} \tag{25}$$

Using the symmetry of the matrices $S(x)$ and $S(x)A_j(x)$, we have

$$\begin{aligned}\frac{d}{dt}\big\|u(.,t)\big\|_S^2 &= -\sum_{j=1}^{d}\big[(\partial_x u,SA_j u)_{L^2} + (u,SA_j\partial_x u)_{L^2}\big] + 2(Su,f)_{L^2}\\ &\quad - 2(SA_0u,u)_{L^2} - 2(SBu,u)_{L^2}.\end{aligned} \tag{26}$$

Integration by parts of the first member of the right hand side yields

$$\frac{d}{dt}\|u(.,t)\|_S^2 = \sum_{j=1}^{d}\big(u, \partial_x(SA_j)u\big)_{L^2} + 2(Su, f)_{L^2} - 2(SA_0u, u)_{L^2} - 2(SBu, u)_{L^2}, \tag{27}$$

as we have assumed a homogeneous Dirichlet boundary condition on $\partial\Omega$. Using the Cauchy–Schwartz inequality on Eq. (27) yields

$$\begin{aligned}\frac{d}{dt}\|u(.,t)\|_S^2 \leq &\left(\sum_{j=1}^{d}\sup_x|\partial_x(SA_j)| + 2\sup_x|SA_0|\right)\|u(.,t)\|_S^2 \\ &+ 2\|u(.,t)\|_S\|f(.,t)\|_S - 2(SBu,u)_{L^2}.\end{aligned} \tag{28}$$

Using the identity

$$\forall(a,b)\in\mathbb{R}^2,\quad ab \leq \frac{1}{2}\big(a^2+b^2\big), \tag{29}$$

we find finally

$$\frac{d}{dt}\|u(.,t)\|_S^2 \leq (\gamma+1)\|u(.,t)\|_S^2 + \|f(.,t)\|_S^2 - 2(SBu,u)_{L^2}, \tag{30}$$

where γ is defined in Eq. (19).

To show that the introduction of B dissipates the energy of the solution, we have to show that the quantity $(SBu,u)_{L^2}$ is positive. We first demonstrate the

Lemma 1. *Let $A\in\mathbb{M}_p(\mathbb{R})$. Let $S\in\mathbb{M}_p(\mathbb{R})$ symmetric positive definite such that SA is symmetric. Then the eigenspaces of A form an orthogonal direct sum for the scalar product induced by S on $\mathbb{R}^p$.*

Proof. Let $(u,v)\in\mathbb{R}^p\times\mathbb{R}^p$ be two eigenvectors of A

$$Au=\lambda u,\qquad Av=\mu v, \tag{31}$$

where λ and μ are the eigenvalues associated with u and v respectively. We have

$$\langle Su, v\rangle = \frac{1}{\lambda}\langle SAu, v\rangle = \frac{1}{\lambda}\langle u, SAv\rangle = \frac{\mu}{\lambda}\langle u, Sv\rangle = \frac{\mu}{\lambda}\langle Su, v\rangle. \tag{32}$$

Therefore, either

$$\langle Su, v\rangle = 0, \tag{33}$$

and the eigenvectors u, v are orthogonal for the scalar product induced by S or

$$\langle Su, v\rangle \neq 0,\qquad \lambda=\mu, \tag{34}$$

which means that u and v belongs to the same eigenspace of A. □

The function $u(x,t)\in L^2(\Omega\times[0,T],\mathbb{R}^p)$ can be decomposed according to the direct sum of the eigenspaces of $A_j(x)$ as

$$\forall(x,t)\in\Omega\times[0,T],\quad u(x,t)=\sum_i \alpha_{j,i}(x,t)a_{j,i}(x). \tag{35}$$

Consider $B^+_{j,1}$, the spectral projector on the eigenspace $\ker(A_j-\lambda_{j,1}I)$, where $I\in\mathbb{M}_p(\mathbb{R})$ is the identity matrix and $\lambda_{j,1}(x)$ the first positive eigenvalue of the matrix $A_j(x)$. We have

$$B^+_{j,1}(x)u(x,t) = \alpha_{j,1}(x,t)a_{j,1}(x). \tag{36}$$

Therefore,

$$\begin{aligned}\big(SB^+_{j,1}u,u\big)_{L^2} &= \int_\Omega \big\langle S(x)B^+_{j,1}(x)u(x,t), u(x,t)\big\rangle dx \\ &= \int_\Omega \left\langle \alpha_{j,1}(x,t)S(x)a_{j,1}(x), \sum_i \alpha_{j,i}(x,t)a_{j,i}(x)\right\rangle dx \\ &= \int_\Omega \sum_i \alpha_{j,1}(x,t)\alpha_{j,i}(x,t)\big\langle S(x)a_{j,1}(x), a_{j,i}(x)\big\rangle dx.\end{aligned} \tag{37}$$

Using Lemma 1, we find

$$\left(SB_{j,1}^{+}u,u\right)_{L^2}=\int_{\Omega}\alpha_{j,1}^{2}(x,t)\left\langle S(x)a_{j,1}(x),a_{j,1}(x)\right\rangle dx. \tag{38}$$

As $S(x)$ is symmetric definite positive, we have

$$\left(SB_{j,1}^{+}u,u\right)_{L^2}\geq 0. \tag{39}$$

The same demonstration is valid for any spectral projectors $B_{j,i}^{+}$, $B_{j,i}^{-}$ on the eigenvalues of A_j. Therefore, as B is a linear combination of these projectors weighted by positive functions $d_j^{\pm}(x_j)$ we have

$$(SBu,u)_{L^2}\geq 0. \qquad \square \tag{40}$$

This property of the SMART layer ensures that the introduction of the layer decreases the energy of the solution. In addition, the energy inequality shows that if the solution has no component propagating in directions for which the absorption term $B(x)$ is defined, then $u(x,t)\in\ker B(x)$ and no dissipation is induced by the layer. On the other hand, as long as $u(x,t)\notin\ker B(x)$, then the dissipation occurs. Therefore, the introduction of the zero-order term associated with the SMART layer strategy has only a dissipative effect: if the system is well-posed, the SMART layer strategy do not yield instabilities, as it can be the case for the PML strategy.

Finally, note that for the sponge layer, it is straightforward to show that the zero-order term which is introduced is also dissipative. From Eq. (14), we have

$$B(x)=\alpha(x)I, \tag{41}$$

therefore

$$(SBu,u)_{L^2}=\int_{\Omega}\alpha(x)\left\langle S(x)u(x),u(x)\right\rangle dx, \tag{42}$$

and $(SBu,u)_{L^2}\geq 0$ as $\alpha(x)\geq 0$.

3. Anisotropic wave equation in 2D TI media

In this section we demonstrate that the elastic VTI system, as well as the acoustic VTI and TTI systems derived from the linear elasticity, are symmetrizable. Therefore, they satisfy the requirements for the SMART layer method to be applied. The symmetrizability of these systems is proven by the explicit construction of symmetrizers. In the general TI case, the definition of the compliance matrix, the inverse of the stiffness tensor, gives an automatic procedure to derive these symmetrizers [12].

Remark concerning the notations. As we focus on the 2D case, in the sequel, the space variable will be now denoted by $(x,z)\in\mathbb{R}^2$. All the subsurface parameters (P-wave velocity, S-wave velocity, density, stiffness tensor coefficients, Thomsen anisotropy parameters, tilt angle) depend on the space variables (x,z), but this dependency is not always written explicitly to alleviate the notations.

3.1. Starting from linear elasticity: the Duveneck and Bakker strategy

3.1.1. 2D wave propagation in elastic VTI media

Let $u(x,z,t)$ be the particle velocity displacement vector, such that

$$u(x,z,t)=\begin{bmatrix}u_x(x,z,t) & u_z(x,z,t)\end{bmatrix}^T. \tag{43}$$

Let $\sigma(x,z,t)$ be the vector of the stress components

$$\sigma(x,z,t)=\begin{bmatrix}\sigma_{xx}(x,z,t) & \sigma_{zz}(x,z,t) & \sigma_{xz}(x,z,t)\end{bmatrix}^T. \tag{44}$$

Let $\varepsilon(x,z,t)$ be the vector of the strain components

$$\varepsilon(x,z,t)=\begin{bmatrix}\varepsilon_{xx}(x,z,t) & \varepsilon_{zz}(x,z,t) & \varepsilon_{xz}(x,z,t)\end{bmatrix}^T. \tag{45}$$

We consider the 2D linear elasticity equations in a VTI medium. The anisotropy symmetry axis is directed following the vertical axis. The standard stress-strain relation is given by the Hooke's law

$$\sigma(x,z,t)=C(x,z)\varepsilon(x,z,t), \tag{46}$$

where the stiffness tensor $C(x,z)$ tensor may be expressed as

$$C(x,z) = \begin{pmatrix} c_{11} & c_{13} & 0 \\ c_{13} & c_{33} & 0 \\ 0 & 0 & c_{44} \end{pmatrix}, \tag{47}$$

using the Voigt notations. The strain components are related to the particle velocity displacements through the equations

$$\begin{cases} \partial_t \varepsilon_{xx} = \partial_x u_x \\ \partial_t \varepsilon_{zz} = \partial_z u_z \\ \partial_t \varepsilon_{xz} = \dfrac{1}{2}(\partial_z u_x + \partial_x u_z). \end{cases} \tag{48}$$

In addition, the particle displacement velocity and the stress are related by the equations of motion

$$\begin{cases} \partial_t u_x = \dfrac{1}{\rho}(\partial_x \sigma_{xx} + \partial_z \sigma_{xz}) \\ \partial_t u_z = \dfrac{1}{\rho}(\partial_z \sigma_{zz} + \partial_x \sigma_{xz}). \end{cases} \tag{49}$$

The first-order velocity-stress system associated with the propagation of elastic waves in 2D VTI media is thus

$$\begin{cases} \partial_t u_x - \dfrac{1}{\rho}\partial_x \sigma_{xx} - \dfrac{1}{\rho}\partial_z \sigma_{xz} = 0 \\ \partial_t u_z - \dfrac{1}{\rho}\partial_z \sigma_{zz} - \dfrac{1}{\rho}\partial_x \sigma_{xz} = 0 \\ \partial_t \sigma_{xx} - c_{11}\partial_x u_x - c_{13}\partial_z u_z = 0 \\ \partial_t \sigma_{zz} - c_{13}\partial_x u_x - c_{33}\partial_z u_z = 0 \\ \partial_t \sigma_{xz} - \dfrac{c_{44}}{2}(\partial_x u_z + \partial_z u_x) = 0. \end{cases} \tag{50}$$

Theorem 2. *The hyperbolic system (50) is symmetrizable.*

Proof. We follow the approach of Burridge [12] to rewrite the system (50) using the compliance matrix $C^{-1}(x,z)$. The stiffness tensor $C(x,z)$ is symmetric positive-definite by definition. Therefore, $C(x,z)$ is invertible, and its inverse $C^{-1}(x,z)$ is symmetric positive-definite. We introduce the matrix

$$M(x,z) = DC^{-1}(x,z)D, \tag{51}$$

where D is the diagonal scaling matrix

$$\begin{pmatrix} 1 & 0 & 0 \\ 0 & 1 & 0 \\ 0 & 0 & 2 \end{pmatrix}. \tag{52}$$

Following the Voigt notations, we introduce the (scaled) stress vector $\sigma = [\sigma_{xx}\ \sigma_{zz}\ \frac{\sigma_{xz}}{2}]$. Combining Eqs. (47), (48) and (51), we obtain the equations

$$M\partial_t \sigma + X_1 \partial_x u + X_2 \partial_z u = 0, \tag{53}$$

where

$$X_1 = -\begin{pmatrix} 1 & 0 \\ 0 & 0 \\ 0 & 1 \end{pmatrix}, \qquad X_2 = -\begin{pmatrix} 0 & 0 \\ 0 & 1 \\ 1 & 0 \end{pmatrix}. \tag{54}$$

The equations of motion can also be rewritten as

$$\rho\partial_t u + X_1^T \partial_x \sigma + X_2^T \partial_z \sigma = 0. \tag{55}$$

Therefore, if we consider the vector $w(x,z,t) = [u(x,z,t)\ \sigma(x,z,t)]^T$ and the matrix

$$S(x,z) = \begin{pmatrix} \rho I & 0 \\ 0 & M \end{pmatrix}, \tag{56}$$

where $I \in \mathbb{M}_2(\mathbb{R})$ is the identity matrix, we obtain the system

$$S\partial_t w + \tilde{X}_1 \partial_x w + \tilde{X}_2 \partial_z w = 0, \tag{57}$$

where

$$\tilde{X}_1 = \begin{pmatrix} 0 & X_1^T \\ X_1 & 0 \end{pmatrix}, \qquad \tilde{X}_2 = \begin{pmatrix} 0 & X_2^T \\ X_2 & 0 \end{pmatrix}. \tag{58}$$

The matrices $\tilde{X}_i$ and $S(x,z)$ are symmetric by construction. In addition, $S(x,z)$ is positive-definite, as it is block diagonal, with each block being symmetric positive-definite.

We thus see that the system (50) may be rewritten under the general form (7) for the unknown $w(x,z,t)$ with matrices

$$A_0(x,z)=0, \qquad A_1(x,z)=S^{-1}(x,z)\tilde{X}_1, \qquad A_2(x,z)=S^{-1}(x,z)\tilde{X}_2. \tag{59}$$

Since the matrices $\tilde{X}_j$, $j=1,2$ are symmetric, the matrix $S(x,z)$ is a symmetric positive definite symmetrizer for the matrices $A_j(x,z)$, $j=1,2$ and the system (50) is symmetrizable. □

3.1.2. Acoustic VTI approximation

The acoustic VTI approximation consists in setting the S-wave velocity to 0 in Eq. (50). We rewrite the stiffness tensor coefficient in function of the Thomsen anisotropy parameters $\epsilon(x,z)$ and $\delta(x,z)$ [42], the vertical P-wave velocity $v_P(x,z)$ the S-wave velocity $v_S(x,z)$, and the density $\rho(x,z)$.

$$\begin{cases} c_{11}=\rho v_P^2(1+2\epsilon), \\ c_{33}=\rho v_P^2, \\ c_{44}=\rho v_S^2, \\ (c_{13}+c_{44})^2=\rho^2\left(v_P^2-v_S^2\right)^2+2\delta\rho^2 v_P^2\left(v_P^2-v_S^2\right). \end{cases} \tag{60}$$

We see that setting v_S to 0 amounts to setting c_{44} to 0. We obtain

$$\begin{cases} \partial_t u_x-\dfrac{1}{\rho}\partial_x\sigma_{xx}=0 \\ \partial_t u_z-\dfrac{1}{\rho}\partial_z\sigma_{zz}=0 \\ \partial_t\sigma_{xx}-\rho v_P^2\left[(1+2\epsilon)\partial_x u_x+\sqrt{1+2\delta}\partial_z u_z\right]=0 \\ \partial_t\sigma_{zz}-\rho v_P^2[\sqrt{1+2\delta}\partial_x u_x+\partial_z u_z]=0. \end{cases} \tag{61}$$

The equation on the shear term σ_{xz} is canceled, and the number of equations is reduced from 5 to 4. As for the previous system, we can prove the following theorem.

Theorem 3. *The hyperbolic VTI acoustic system (61) is symmetrizable.*

Proof. Consider the reduced stiffness tensor $C_r(x,z)$ resulting from the acoustic VTI approximation

$$C_r(x,z)=\begin{pmatrix} c_{11} & c_{13} \\ c_{13} & c_{33} \end{pmatrix}=\rho v_P^2\begin{pmatrix} 1+2\epsilon & \sqrt{1+2\delta} \\ \sqrt{1+2\delta} & 1 \end{pmatrix}. \tag{62}$$

The eigenvalues of $C_r(x,z)$ are

$$\lambda_1(x,z)=\epsilon+1-\sqrt{\epsilon^2+2\delta+1}, \qquad \lambda_2(x,z)=\epsilon+1+\sqrt{\epsilon^2+2\delta+1}. \tag{63}$$

- In the general case $\epsilon(x,z)>\delta(x,z)$, $C_r(x,z)$ is positive definite (therefore invertible), as its eigenvalues are strictly positive. In this case we can define the reduced compliance matrix $M_r(x,z)=C_r^{-1}(x,z)$ and the symmetrizability of the system (61) can be shown following the same process as for the system (50).
- The case $\epsilon(x,z)=\delta(x,z)$ is referred to as elliptical anisotropy, for which $C_r(x,z)$ is positive but not definite, and therefore not invertible. We show that the system (50) is reduced in this case to a system of three equations which is symmetrizable.
- The case $\epsilon(x,z)<\delta(x,z)$ is excluded, as it corresponds to non-physical imaginary eigenvalues of the reduced stiffness tensor $C_r(x,z)$.

We first consider the general case $\epsilon(x,z)>\delta(x,z)$. Introducing the reduced stress vector $\sigma_r(x,z,t)=[\sigma_{xx}(x,z,t),\ \sigma_{zz}(x,z,t)]$, the tensor $C_r(x,z)$ relates $\sigma_r(x,z,t)$ and the velocity displacement vector $u(x,z,t)$ through the relation

$$\partial_t\sigma_r=C_rX_1\partial_x u+C_rX_2\partial_z u, \tag{64}$$

where

$$X_1=\begin{pmatrix} 1 & 0 \\ 0 & 0 \end{pmatrix}, \qquad X_2=\begin{pmatrix} 0 & 0 \\ 0 & 1 \end{pmatrix}. \tag{65}$$

The system (61) can thus be written in the form

$$\begin{cases} \rho\partial_t u+X_1\partial_x u+X_2\partial_z u=0 \\ M_r\partial_t\sigma+X_1\partial_x u+X_2\partial_z u=0. \end{cases} \tag{66}$$

Introducing as previously $w = [u\ \sigma]^T$, the system (66) is equivalent to the system

$$S\partial_t w + \tilde{X}_1 \partial_x w + \tilde{X}_2 \partial_z w = 0, \tag{67}$$

where

$$S(x,z) = \begin{pmatrix} \rho I & 0 \\ 0 & M \end{pmatrix}, \qquad \tilde{X}_1 = \begin{pmatrix} 0 & X_1 \\ X_1 & 0 \end{pmatrix}, \qquad \tilde{X}_2 = \begin{pmatrix} 0 & X_2 \\ X_2 & 0 \end{pmatrix}, \tag{68}$$

with $I \in \mathbb{M}_2(\mathbb{R})$ the identity matrix. As an inverse of a symmetric positive-definite matrix, $M_r(x,z)$ is itself symmetric positive-definite, and therefore $S(x,z)$ is symmetric positive-definite. Moreover, the matrices $\tilde{X}_1$ and $\tilde{X}_2$ are symmetric, as X_1 and X_2 are symmetric. Thus the system (61) can be written in the general form (7) with $A_0(x,z) = 0$ and

$$\begin{aligned} A_1(x,z) &= S^{-1}(x,z)\tilde{X}_1 = \begin{pmatrix} 0 & 0 & -1/\rho & 0 \\ 0 & 0 & 0 & 0 \\ -\rho v_P^2(1+2\epsilon) & 0 & 0 & 0 \\ -\rho v_P^2\sqrt{1+2\delta} & 0 & 0 & 0 \end{pmatrix}, \\ A_2(x,z) &= S^{-1}(x,z)\tilde{X}_2 = \begin{pmatrix} 0 & 0 & 0 & 0 \\ 0 & 0 & 0 & -1/\rho \\ -\rho v_P^2\sqrt{1+2\delta} & 0 & 0 & 0 \\ -\rho v_P^2 & 0 & 0 & 0 \end{pmatrix}. \end{aligned} \tag{69}$$

The matrix $S(x,z)$ is thus a symmetrizer for the matrices $A_j(x,z)$, $j = 1,2$ and the system (61) is symmetrizable.

We now consider the particular case of elliptical anisotropy $\epsilon(x,z) = \delta(x,z)$. We define the quantity $p(x,z,t)$ as

$$p(x,z,t) = \frac{\sigma_{xx}(x,z,t)}{\sqrt{1+2\epsilon}}. \tag{70}$$

The system (61) reduces to

$$\begin{cases} \partial_t u_x - \dfrac{\sqrt{1+2\epsilon}}{\rho}\partial_x p - \dfrac{\partial_x(\sqrt{1+2\epsilon})}{\rho} u_x = 0 \\ \partial_t u_z - \dfrac{1}{\rho}\partial_z p = 0 \\ \partial_t p - \rho v_P^2[\sqrt{1+2\epsilon}\partial_x u_x + \partial_z u_z] = 0, \end{cases} \tag{71}$$

which can be rewritten under the general formulation (7) with

$$\begin{aligned} A_0(x,z) &= \begin{pmatrix} -\frac{\partial_x(\sqrt{1+2\epsilon})}{\rho} & 0 & 0 \\ 0 & 0 & 0 \\ 0 & 0 & 0 \end{pmatrix}, \qquad A_1(x,z) = \begin{pmatrix} 0 & 0 & \frac{\sqrt{1+2\epsilon}}{\rho} \\ 0 & 0 & 0 \\ \rho v_P^2\sqrt{1+2\epsilon} & 0 & 0 \end{pmatrix}, \\ A_2(x,z) &= \begin{pmatrix} 0 & 0 & 0 \\ 0 & 0 & \frac{1}{\rho} \\ 0 & \rho v_P^2 & 0 \end{pmatrix}. \end{aligned} \tag{72}$$

In this case, a common symmetrizer to the matrices $A_j(x,z)$, $j = 1,2$, is

$$S(x,z) = \begin{pmatrix} \rho & 0 & 0 \\ 0 & \rho & 0 \\ 0 & 0 & \frac{1}{\rho v_P^2} \end{pmatrix}. \tag{73}$$

Note that $S(x,z)$ is also a symmetrizer for the 2D acoustic equations written as a first-order hyperbolic system (velocity-stress formulation). □

3.1.3. Acoustic TTI approximation

The system (61) can be generalized to a medium for which the anisotropy symmetry axis is tilted from an angle θ from the vertical axis. In the general case this angle may depend locally on the subsurface structure, therefore, we consider θ as a function of x and z

$$\theta = \theta(x,z). \tag{74}$$

The introduction of this local tilt angle requires to define a local rotated system along which the anisotropy symmetry axis is aligned. We introduce the rotation matrix $R_\theta(x,z)$ such that

$$R_\theta(x,z) = \begin{pmatrix} \cos\theta & -\sin\theta \\ \sin\theta & \cos\theta \end{pmatrix}. \tag{75}$$

Note that the Hooke's law expressing the anisotropy is now defined in the locally rotated coordinates system. We thus introduce the rotated stress and strain tensors

$$\hat{\sigma}^{\theta}(x,z,t) = R_{\theta}\hat{\sigma}R_{\theta}^{T}, \qquad \hat{\varepsilon}^{\theta}(x,z,t) = R_{\theta}\hat{\varepsilon}R_{\theta}^{T}, \tag{76}$$

where $\hat{\sigma}(x,z,t)$ and $\hat{\varepsilon}(x,z,t)$ are the stress and strain tensors under their matrix form

$$\hat{\sigma}(x,z,t) = \begin{pmatrix} \sigma_{xx} & \sigma_{xz} \\ \sigma_{xz} & \sigma_{zz} \end{pmatrix}, \qquad \hat{\varepsilon}(x,z,t) = \begin{pmatrix} \varepsilon_{xx} & \varepsilon_{xz} \\ \varepsilon_{xz} & \varepsilon_{zz} \end{pmatrix}. \tag{77}$$

Due to the acoustic TTI anisotropy assumption, the rotated tensors $\hat{\sigma}^{\theta}(x,z,t)$ and $\hat{\varepsilon}^{\theta}(x,z,t)$ are diagonal: the off-diagonal elements $\sigma_{xz}^{\theta}(x,z,t)$ and $\varepsilon_{xz}^{\theta}(x,z,t)$ are 0. We can thus introduce the vectors $\sigma^{\theta}(x,z,t)$ and $\varepsilon^{\theta}(x,z,t)$ as

$$\sigma^{\theta}(x,z,t) = \begin{bmatrix} \sigma_{xx}^{\theta} & \sigma_{zz}^{\theta} \end{bmatrix}^{T}, \qquad \varepsilon^{\theta}(x,z,t) = \begin{bmatrix} \varepsilon_{xx}^{\theta} & \varepsilon_{zz}^{\theta} \end{bmatrix}^{T}, \tag{78}$$

following the Voigt notations. They are related through the equation

$$\sigma^{\theta}(x,z,t) = C_r(x,z)\varepsilon^{\theta}(x,z,t), \tag{79}$$

where $C_r(x,z)$ is the reduced stiffness tensor introduced in Eq. (62). Developing this equation yields

$$\begin{cases} \sigma_{xx}^{\theta} = \rho v_P^2\big[(1+2\epsilon)\varepsilon_{xx}^{\theta} + \sqrt{1+2\delta}\varepsilon_{zz}^{\theta}\big] \\ \sigma_{zz}^{\theta} = \rho v_P^2\big[\sqrt{1+2\delta}\varepsilon_{xx}^{\theta} + \varepsilon_{zz}^{\theta}\big]. \end{cases} \tag{80}$$

From Eq. (76) we have

$$\begin{cases} \varepsilon_{xx}^{\theta} = \cos^2\theta\varepsilon_{xx} - 2\sin\theta\cos\theta\varepsilon_{xz} + \sin^2\theta\varepsilon_{zz} \\ \varepsilon_{zz}^{\theta} = \sin^2\theta\varepsilon_{xx} + 2\sin\theta\cos\theta\varepsilon_{xz} + \cos^2\theta\varepsilon_{zz}. \end{cases} \tag{81}$$

Using Eqs. (48), we can express the relation between the rotated stress tensor $\sigma^{\theta}(x,z)$ and the particle velocity displacement $u(x,z)$

$$\begin{cases} \partial_t\sigma_{xx}^{\theta} = \rho v_P^2(1+2\epsilon)\big[\cos^2\theta\partial_x u_x - \sin\theta\cos\theta(\partial_x u_z + \partial_z u_x) + \sin^2\theta\partial_z u_z\big] \\ \qquad\qquad + \rho v_P^2\sqrt{1+2\delta}\big[\sin^2\theta\partial_x u_x + \sin\theta\cos\theta(\partial_x u_z + \partial_z u_x) + \cos^2\theta\partial_z u_z\big] \\ \partial_t\sigma_{zz}^{\theta} = \rho v_P^2\sqrt{1+2\delta}\big[\cos^2\theta\partial_x u_x - \sin\theta\cos\theta(\partial_x u_z + \partial_z u_x) + \sin^2\theta\partial_z u_z\big] \\ \qquad\qquad + \rho v_P^2\big[\sin^2\theta\partial_x u_x + \sin\theta\cos\theta(\partial_x u_z + \partial_z u_x) + \cos^2\theta\partial_z u_z\big]. \end{cases} \tag{82}$$

In addition, using relation (76) we can express the components of the stress tensor in the non-rotated coordinate system

$$\begin{cases} \sigma_{xx} = \cos^2\theta\sigma_{xx}^{\theta} + \sin^2\theta\sigma_{zz}^{\theta} \\ \sigma_{xz} = \sin\theta\cos\theta\big(\sigma_{zz}^{\theta} - \sigma_{xx}^{\theta}\big) \\ \sigma_{zz} = \sin^2\theta\sigma_{xx}^{\theta} + \cos^2\theta\sigma_{zz}^{\theta}. \end{cases} \tag{83}$$

Combining (83) with the equation of motion (49), we obtain

$$\begin{cases} \partial_t u_x = \dfrac{1}{\rho}\big[\partial_x\big(\cos^2\theta\sigma_{xx}^{\theta} + \sin^2\theta\sigma_{zz}^{\theta}\big) + \partial_z\big(\sin\theta\cos\theta\big(\sigma_{zz}^{\theta} - \sigma_{xx}^{\theta}\big)\big)\big] \\ \partial_t u_z = \dfrac{1}{\rho}\big[\partial_z\big(\sin^2\theta\sigma_{xx}^{\theta} + \cos^2\theta\sigma_{zz}^{\theta}\big) + \partial_x\big(\sin\theta\cos\theta\big(\sigma_{zz}^{\theta} - \sigma_{xx}^{\theta}\big)\big)\big], \end{cases} \tag{84}$$

and we end up with the general TTI acoustic first-order system

$$\begin{cases} \partial_t u_x = \dfrac{1}{\rho}\big[\partial_x\big(\cos^2\theta\sigma_{xx}^{\theta} + \sin^2\theta\sigma_{zz}^{\theta}\big) + \partial_z\big(\sin\theta\cos\theta\big(\sigma_{zz}^{\theta} - \sigma_{xx}^{\theta}\big)\big)\big] \\ \partial_t u_z = \dfrac{1}{\rho}\big[\partial_z\big(\sin^2\theta\sigma_{xx}^{\theta} + \cos^2\theta\sigma_{zz}^{\theta}\big) + \partial_x\big(\sin\theta\cos\theta\big(\sigma_{zz}^{\theta} - \sigma_{xx}^{\theta}\big)\big)\big] \\ \partial_t\sigma_{xx}^{\theta} = \rho v_P^2(1+2\epsilon)\big[\cos^2\theta\partial_x u_x - \sin\theta\cos\theta(\partial_x u_z + \partial_z u_x) + \sin^2\theta\partial_z u_z\big] \\ \qquad\qquad + \rho v_P^2\sqrt{1+2\delta}\big[\sin^2\theta\partial_x u_x + \sin\theta\cos\theta(\partial_x u_z + \partial_z u_x) + \cos^2\theta\partial_z u_z\big] \\ \partial_t\sigma_{zz}^{\theta} = \rho v_P^2\sqrt{1+2\delta}\big[\cos^2\theta\partial_x u_x - \sin\theta\cos\theta(\partial_x u_z + \partial_z u_x) + \sin^2\theta\partial_z u_z\big] \\ \qquad\qquad + \rho v_P^2\big[\sin^2\theta\partial_x u_x + \sin\theta\cos\theta(\partial_x u_z + \partial_z u_x) + \cos^2\theta\partial_z u_z\big]. \end{cases} \tag{85}$$

Theorem 4. *The hyperbolic system (85) is symmetrizable.*

Proof. As for the acoustic VTI system (61), we have to distinguish the general case $\epsilon(x,z) > \delta(x,z)$ and the elliptical case $\epsilon(x,z) = \delta(x,z)$.

We start with the general case. In this case, the reduced stiffness tensor $C_r(x,z)$ can be inverted. We introduce the matrices

$$X_1^\theta(x,z) = -\begin{pmatrix} \cos^2\theta & \sin^2\theta \\ -\sin\theta\cos\theta & \sin\theta\cos\theta \end{pmatrix}, \qquad X_2^\theta(x,z) = -\begin{pmatrix} \sin\theta\cos\theta & -\sin\theta\cos\theta \\ \sin^2\theta & \cos^2\theta \end{pmatrix}. \tag{86}$$

The system (85) is equivalent to the system

$$\begin{cases} \rho\partial_t u + \partial_x\big(X_1^\theta\sigma^\theta\big) + \partial_z\big(X_2^\theta\sigma^\theta\big) = 0 \\ M_r\partial_t\sigma^\theta + \big(X_1^\theta\big)^T\partial_x u + \big(X_2^\theta\big)^T\partial_z u = 0 \end{cases} \tag{87}$$

where $M_r(x,z) = C_r^{-1}(x,z)$ is the reduced compliance matrix. Defining

$$w(x,z,t) = \big[u(x,z,t) \quad \sigma^\theta(x,z,t)\big]^T, \tag{88}$$

we can rewrite (85) as

$$S\partial_t w + \tilde{X}_1^\theta\partial_x w + \tilde{X}_2^\theta\partial_z w + \tilde{X}_0^\theta w = 0, \tag{89}$$

where

$$S(x,z) = \begin{pmatrix} \rho I & 0 \\ 0 & M_r \end{pmatrix}, \qquad \tilde{X}_1^\theta(x,z) = \begin{pmatrix} 0 & X_1^\theta \\ (X_1^\theta)^T & 0 \end{pmatrix}, \qquad \tilde{X}_2^\theta(x,z) = \begin{pmatrix} 0 & X_2^\theta \\ (X_2^\theta)^T & 0 \end{pmatrix}, \tag{90}$$

and the zero-order term $\tilde{X}_0^\theta(x,z)$ is

$$\tilde{X}_0^\theta(x,z) = \begin{pmatrix} 0 & \partial_x X_1^\theta + \partial_z X_2^\theta \\ 0 & 0 \end{pmatrix}. \tag{91}$$

Therefore, we can express the system (85) in the general form (7) with

$$\begin{cases} A_0(x,z) = S^{-1}(x,z)X_0^\theta(x,z), \quad A_1(x,z) = S^{-1}(x,z)X_1^\theta(x,z), \\ A_2(x,z) = S^{-1}(x,z)X_2^\theta(x,z). \end{cases} \tag{92}$$

The matrix $S(x,z)$ is as symmetric positive-definite symmetrizer for this system, which is symmetrizable.

In the case of elliptical anisotropy, the reduced stiffness tensor is not invertible. However, as for the acoustic VTI equations, we can define

$$p^\theta(x,z,t) = \frac{\sigma^\theta(x,z,t)}{\sqrt{1+\epsilon}}, \tag{93}$$

and the system (85) reduces to

$$\begin{cases} \partial_t u_x &= \dfrac{1}{\rho}\big[\partial_x\big(\cos^2\theta\sqrt{1+2\epsilon}\,p^\theta + \sin^2\theta\, p^\theta\big) + \partial_z\big(\sin\theta\cos\theta(1-\sqrt{1+2\epsilon}\,)p^\theta\big)\big] \\ \partial_t u_z &= \dfrac{1}{\rho}\big[\partial_z\big(\sin^2\theta\sqrt{1+2\epsilon}\,p^\theta + \cos^2\theta\, p^\theta\big) + \partial_x\big(\sin\theta\cos\theta(1-\sqrt{1+2\epsilon}\,)p^\theta\big)\big] \\ \partial_t p^\theta &= \rho v_P^2\sqrt{1+2\epsilon}\big[\cos^2\theta\partial_x u_x - \sin\theta\cos\theta(\partial_x u_z + \partial_z u_x) + \sin^2\theta\partial_z u_z\big] \\ &\quad + \rho v_P^2\big[\sin^2\theta\partial_x u_x + \sin\theta\cos\theta(\partial_x u_z + \partial_z u_x) + \cos^2\theta\partial_z u_z\big]. \end{cases} \tag{94}$$

We can rewrite the system (94) under the general form (7) with

$$A_0(x,z) = \begin{pmatrix} 0 & 0 & \frac{\partial_x\mu + \partial_z\nu}{\rho} \\ 0 & 0 & \frac{\partial_x\mu + \partial_z\nu}{\rho} \\ 0 & 0 & 0 \end{pmatrix}, \qquad A_1(x,z) = -\begin{pmatrix} 0 & 0 & \frac{\mu}{\rho} \\ 0 & 0 & \frac{\nu}{\rho} \\ \rho v_P^2\mu & \rho v_P^2\nu & 0 \end{pmatrix},$$
$$A_2(x,z) = -\begin{pmatrix} 0 & 0 & \frac{\nu}{\rho} \\ 0 & 0 & \frac{\mu}{\rho} \\ \rho v_P^2\nu & \rho v_P^2\mu & 0 \end{pmatrix}, \tag{95}$$

where

$$\mu(x,z) = \left(\cos^2\theta\sqrt{1+2\epsilon} + \sin^2\theta\right), \qquad \nu(x,z) = \left(\sin\theta\cos\theta(1-\sqrt{1+2\epsilon})\right). \tag{96}$$

A symmetrizer for the system (94) is thus

$$S(x,z) = \begin{pmatrix} \rho & 0 & 0 \\ 0 & \rho & 0 \\ 0 & 0 & \frac{1}{\rho v_P^2} \end{pmatrix}, \tag{97}$$

which is the same as the one introduced for the VTI elliptical case (and a symmetrizer for the 2D acoustic equations). □

The elastic VTI system and the acoustic TI hyperbolic systems derived from this system are thus symmetrizable. The symmetrizers can be built explicitly from the compliance matrix, following the approach of Burridge [12].

4. Numerical results

In the next section, we investigate the numerical properties of the SMART layer method and compare it to the PML and sponge layer methods when applied to the 2D acoustic TTI system (85).

4.1. Framework and implementation details

4.1.1. SMART layer

The implementation of the SMART layer strategy requires to compute the projectors on the eigenspaces of the matrices $A_j(x,z)$, $j=1,2$ of Eq. (95). In the general case $\epsilon(x,z) > \delta(x,z)$, the non-zero eigenvalues of $A_1(x,z)$ are

$$\lambda_{1P}^{\pm}(x,z) = \pm v_P\sqrt{\frac{a_1+\sqrt{\Delta_1}}{2}}, \qquad \lambda_{1S}^{\pm}(x,z) = \pm v_P\sqrt{\frac{a_1-\sqrt{\Delta_1}}{2}}, \tag{98}$$

where

$$a_1(x,z) = 1+2\epsilon\cos^2\theta, \qquad \Delta_1(x,z) = \left((1+2\epsilon)\cos^2\theta + \sin^2\theta\right)^2 + 8(\epsilon-\delta)\cos^2\theta\sin^2\theta. \tag{99}$$

Similarly, the eigenvalues of $A_2(x,z)$ are

$$\lambda_{2P}^{\pm}(x,z) = \pm v_P\sqrt{\frac{a_2+\sqrt{\Delta_2}}{2}}, \qquad \lambda_{2S}^{\pm}(x,z) = \pm v_P\sqrt{\frac{a_2-\sqrt{\Delta_2}}{2}}, \tag{100}$$

where

$$a_2(x,z) = 1+2\epsilon\sin^2\theta, \qquad \Delta_2(x,z) = \left((1+2\epsilon)\sin^2\theta + \cos^2\theta\right)^2 + 8(\epsilon-\delta)\cos^2\theta\sin^2\theta. \tag{101}$$

The multiplicity of these eigenvalues is 1. The projectors $B_{jP}^{\pm}(x,z)$, $B_{jS}^{\pm}(x,z)$ associated with the eigenvalues $\lambda_{jP}^{\pm}(x,z)$, $\lambda_{jS}^{\pm}(x,z)$ are thus defined as

$$B_{jP}^{\pm}(x,z) = \frac{v_{jP}^{\pm}(v_{jP}^{\pm})^T}{\|v_{jP}^{\pm}\|^2}, \qquad B_{jS}^{\pm}(x,z) = \frac{v_j S^{\pm}(v_{jS}^{\pm})^T}{\|v_{jS}^{\pm}\|^2}, \tag{102}$$

where $v_{jP}^{\pm}(x,z)$, $v_{jS}^{\pm}(x,z)$ are the eigenvectors of $A_j(x,z)$ associated with $\lambda_{jP}^{\pm}(x,z)$ and $\lambda_{jS}^{\pm}(x,z)$. For the system (85) we can show that these eigenvectors are

$$v_{jP}^{\pm}(x,z) = \begin{bmatrix} \beta \\ \gamma_{jP}^{\pm} \\ \frac{1}{\lambda_{jP}^{\pm}}((A_j)_{31}\beta + (A_j)_{32}\gamma_{jP}^{\pm}) \\ \frac{1}{\lambda_{jP}^{\pm}}((A_j)_{41}\beta + (A_j)_{42}\gamma_{jP}^{\pm}) \end{bmatrix}, \qquad v_{jS}^{\pm}(x,z) = \begin{bmatrix} \beta \\ \gamma_{jS}^{\pm} \\ \frac{1}{\lambda_{jS}^{\pm}}((A_j)_{31}\beta + (A_j)_{32}\gamma_{jS}^{\pm}) \\ \frac{1}{\lambda_{jS}^{\pm}}((A_j)_{41}\beta + (A_j)_{42}\gamma_{jS}^{\pm}) \end{bmatrix}, \tag{103}$$

where

$$\begin{cases} \beta(x,z) = (A_j)_{13}(A_j)_{32} + (A_j)_{14}(A_j)_{42} \\ \gamma_{jP}^{\pm}(x,z) = {\lambda_{jP}^{\pm}}^2 - (A_j)_{13}(A_j)_{31} - (A_j)_{14}(A_j)_{41} \\ \gamma_{jS}^{\pm}(x,z) = {\lambda_{jS}^{\pm}}^2 - (A_j)_{13}(A_j)_{31} - (A_j)_{14}(A_j)_{41}. \end{cases} \tag{104}$$

The implementation of the SMART layer only requires to compute the projectors $B^{\pm}_{jP}(x,z)$, $B^{\pm}_{jS}(x,z)$ as the final zero-order operator added to the system (85) is a linear combination of these projectors, as given in Eq. (13). This computation can be done "offline": the projectors depend only on the physical characteristics of the media, which do not depend on the time variable. Therefore, the computation of the zero-order terms associated with the SMART layer are performed as a pre-computation step and does not require additional computation during the time loop.

4.1.2. PML

The standard PML strategy [9] first requires to split the variables. We thus consider the set of variables

$$u = \big[u_{x1}, \quad u_{x2}, \quad u_{z1}, \quad u_{z2}, \quad \sigma^{\theta}_{xx1}, \quad \sigma^{\theta}_{xx2}, \quad \sigma^{\theta}_{zz1}, \quad \sigma^{\theta}_{zz2}\big]^T, \tag{105}$$

where

$$\begin{cases} u_x = u_{x1} + u_{x2}, & \sigma^{\theta}_{xx} = \sigma^{\theta}_{xx1} + \sigma^{\theta}_{xx2} \\ u_z = u_{z1} + u_{z2}, & \sigma^{\theta}_{zz} = \sigma^{\theta}_{zz1} + \sigma^{\theta}_{zz2}. \end{cases} \tag{106}$$

Each equation of the initial system (85) is split in two, and we obtain an 8 equations system such that each equation contains only derivatives in one spatial direction. Based on the definition of the damping coefficients $d^{\pm}_j(x_j)$, $j = 1, 2$ given in Eq. (12) we define the PML damping coefficients $d_x(x)$ and $d_z(z)$ such that

$$d_x(x) = d^+_1(x) + d^-_1(x), \qquad d_z(z) = d^+_2(z) + d^-_2(z). \tag{107}$$

Zero-order terms are added to each of the 8 equations, and we end-up with the PML system

$$\begin{cases} \partial_t u_{x1} + d_x(x) u_{x1} &= \dfrac{1}{\rho}\partial_x\big(\cos^2\theta\,(\sigma^{\theta}_{xx1} + \sigma^{\theta}_{xx2})\big) + \dfrac{1}{\rho}\partial_x\big(\sin^2\theta\,(\sigma^{\theta}_{zz1} + \sigma^{\theta}_{zz2})\big) \\ \partial_t u_{x2} + d_z(z) u_{x2} &= \dfrac{1}{\rho}\partial_z\big(\sin\theta\cos\theta\,(\sigma^{\theta}_{zz1} + \sigma^{\theta}_{zz2})\big) - \dfrac{1}{\rho}\partial_z\big(\sin\theta\cos\theta\,(\sigma^{\theta}_{xx1} + \sigma^{\theta}_{xx2})\big) \\ \partial_t u_{z1} + d_x(x) u_{z1} &= \dfrac{1}{\rho}\partial_x\big(\sin\theta\cos\theta\,(\sigma^{\theta}_{zz1} + \sigma^{\theta}_{zz2})\big) - \dfrac{1}{\rho}\partial_x\big(\sin\theta\cos\theta\,(\sigma^{\theta}_{xx1} + \sigma^{\theta}_{xx2})\big) \\ \partial_t u_{z2} + d_z(z) u_{z2} &= \dfrac{1}{\rho}\partial_z\big(\sin^2\theta\,(\sigma^{\theta}_{xx1} + \sigma^{\theta}_{xx2})\big) + \dfrac{1}{\rho}\partial_z\big(\cos^2\theta\,(\sigma^{\theta}_{zz1} + \sigma^{\theta}_{zz2})\big) \\ \partial_t \sigma^{\theta}_{xx1} + d_x(x)\sigma^{\theta}_{xx1} &= \rho v_P^2\big[(1+2\epsilon)\cos^2\theta + \sqrt{1+2\delta}\sin^2\theta\big]\partial_x(u_{x1}+u_{x2}) \\ &\quad + \rho v_P^2\big[\sqrt{1+2\delta} - (1+2\epsilon)\big]\sin\theta\cos\theta\,\partial_x(u_{z1}+u_{z2}) \\ \partial_t \sigma^{\theta}_{xx2} + d_z(z)\sigma^{\theta}_{xx2} &= \rho v_P^2\big[\sqrt{1+2\delta} - (1+2\epsilon)\big]\sin\theta\cos\theta\,\partial_z(u_{x1}+u_{x2}) \\ &\quad + \rho v_P^2\big[(1+2\epsilon)\sin^2\theta + \sqrt{1+2\delta}\cos^2\theta\big]\partial_z(u_{z1}+u_{z2}) \\ \partial_t \sigma^{\theta}_{zz1} + d_x(x)\sigma^{\theta}_{zz1} &= \rho v_P^2\big[\sqrt{1+2\delta}\cos^2\theta + \sin^2\theta\big]\partial_x(u_{x1}+u_{x2}) \\ &\quad + \rho v_P^2[1 - \sqrt{1+2\delta}\,]\sin\theta\cos\theta\,\partial_x(u_{z1}+u_{z2}) \\ \partial_t \sigma^{\theta}_{zz2} + d_z(z)\sigma^{\theta}_{zz2} &= \rho v_P^2[1 - \sqrt{1+2\delta}\,]\sin\theta\cos\theta\,\partial_z(u_{x1}+u_{x2}) \\ &\quad + \rho v_P^2\big[\sqrt{1+2\delta}\sin^2\theta + \cos^2\theta\big]\partial_z(u_{z1}+u_{z2}). \end{cases} \tag{108}$$

4.1.3. Choice of the damping coefficients

The choice of the damping coefficient is made according to the study of Hu [28] such that

$$d^-_j(x_j) = \frac{8(n+1)}{L_j}\left(\frac{a_j - x_j}{L_j}\right)^n, \qquad d^+_j(x_j) = \frac{8(n+1)}{L_j}\left(\frac{x_j - b_j}{L_j}\right)^n, \tag{109}$$

where $n \in \mathbb{N}$. In the numerical experiments we choose third order polynomials and set n to 3.

4.1.4. Source implementation

The source which is used in the numerical experiments is an explosive Ricker source located at (x_S, z_S), of the form

$$s(x,z,t) = \delta(x - x_S)\delta(z - z_S)\varphi(t), \tag{110}$$

where $\delta(x)$ is the Dirac delta function in space, and

$$\varphi(t) = \big[1 - 2\omega^2(t - t_0)^2\big]e^{-\omega^2(t-t_0)^2}, \quad \omega = \Pi f. \tag{111}$$

In the formula (111) f is the central frequency of the Ricker.

In TI media such that $\epsilon > \delta$, the S-wave velocity is 0 only in the direction of anisotropy symmetry axis and S-waves are generated [24]. However, the acoustic anisotropic wave propagation systems are derived in order to predict correctly the propagation of P-waves in anisotropic media and neglect the propagation of S-waves. The S-waves simulated are thus considered as spurious artifacts. In order to mitigate the amplitude of these S-waves, the introduction of the source is implemented following the strategy proposed by Operto et al. [38]. This leads to the definition of weights $(w_x, w_z) \in \mathbb{R}^2$ such that

$$\begin{cases} w_x = \dfrac{1+2\epsilon+\sqrt{1+2\delta}}{1+\epsilon+\sqrt{1+2\delta}} \\ w_z = \dfrac{1+\sqrt{1+2\delta}}{1+\epsilon+\sqrt{1+2\delta}}. \end{cases} \tag{112}$$

Under the general formulation (9), the source term $f_{SMART}(x,z,t)$ for the SMART layer is thus

$$f_{SMART}(x,z,t) = \begin{bmatrix} 0 & 0 & w_x s & w_z s \end{bmatrix}^T \in \mathbb{R}^4, \tag{113}$$

while for the PML, the source term $f_{PML}(x,z,t)$ is

$$f_{PML}(x,z,t) = \begin{bmatrix} 0 & 0 & 0 & 0 & \dfrac{w_x s}{2} & \dfrac{w_x s}{2} & \dfrac{w_z s}{2} & \dfrac{w_z s}{2} \end{bmatrix}^T \in \mathbb{R}^8. \tag{114}$$

4.1.5. Discretization

We use a finite-difference method to perform the discretization of both systems (85) and (108). The standard staggered grid technique used in electromagnetism [46] and seismic modeling [43] is not adapted as it would require averaging method to estimate the quantities $\partial_x u_z(x,z,t)$ and $\partial_z u_x(x,z,t)$ which are involved in the stress equations. We thus prefer to use the rotated staggered grid technique promoted by Saenger et al. [40]. The velocity displacement fields $u_x(x,z,t)$ and $u_z(x,z,t)$ are discretized over the same grid. This grid is shifted from half a step in both x and z direction from the grid where the stress fields $\sigma^{\theta}_{xx}(x,z,t)$ and $\sigma^{\theta}_{zz}(x,z,t)$ are discretized. The leading idea is to approximate the derivatives along directions $\tilde{x}$ and $\tilde{z}$ rotated from x, z by an angle of 45°.

$$\tilde{x} = \frac{1}{\sqrt{2}}(z+x), \qquad \tilde{z} = \frac{1}{\sqrt{2}}(z-x), \tag{115}$$

and approximate the derivatives along x and z by

$$\partial_x = \frac{1}{\sqrt{2}}(\partial_{\tilde{z}} + \partial_{\tilde{x}}), \qquad \partial_z = \frac{1}{\sqrt{2}}(\partial_{\tilde{z}} - \partial_{\tilde{x}}). \tag{116}$$

In the numerical experiments presented in this section, a 4th order discretization in space and a 2nd order discretization in time is implemented.

4.2. Accuracy comparison between PML, sponge layers and SMART layers

We first perform an accuracy comparison in terms of layer reflectivity, between PML, sponges layers, and SMART layers. We consider a homogeneous domain characterized by the physical parameters

- $v_P = 2000\ \mathrm{m\,s^{-1}}$, $\rho = 1000\ \mathrm{kg\,m^{-3}}$,
- $\epsilon = \delta = 0.3$ (elliptical case),
- $\theta = 36°$.

In this elliptical anisotropy context, the PML is not amplifying, and we can focus on comparing the accuracy of the three different layer methods.

The domain is a 2000 m by 2000 m square. We set the simulation length to 3 s. The source is laterally centered, and located close to the top of the model, such that $x_S = 1000$ m, $z_S = 50$ m. A free-surface condition is implemented at $z = 0$ m: the absorbing layers are defined only at the bottom and at the two lateral sides of the computational domain. The dominant frequency for the source is $f = 15$ Hz. The spatial discretization steps are $\Delta x = 10$ m, $\Delta z = 10$ m, to ensure at least 4 points by minimum wavelength (according to the choice of a 4th order finite-difference scheme in space). The time discretization step is selected so as to satisfy the CFL condition [33].

$$\Delta t \leq \frac{1}{\sqrt{2}\|v_P\|_\infty \sqrt{\frac{1}{\Delta x^2} + \frac{1}{\Delta z^2}}} \tag{117}$$

We first compute a reference solution in an extended domain, sufficiently large to ensure no reflections at its boundaries during the simulation length. We record a reference seismogram using an array of receivers located near the free-surface, at the same depth as the source $z_S = 50$ m, spread along the interval $[a_1, b_1]$, equally spaced each discretization step Δx.

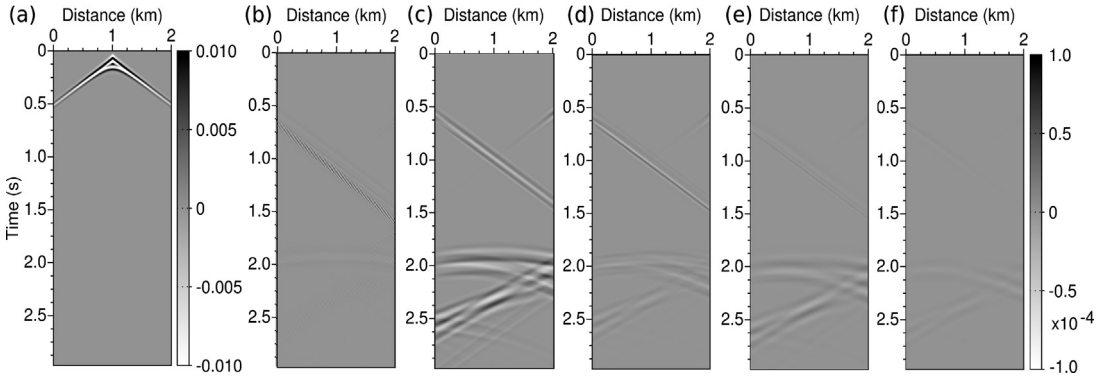

Fig. 1. Elliptical case ($\epsilon = \delta$). Reference seismogram (a). Differential seismogram for PML layers with 1.1 dominant wavelength (b). Differential seismogram for sponge layers with 1.1 dominant wavelength (c). Differential seismogram for SMART layers with 1.1 dominant wavelength (d). Differential seismogram for sponge layers with 1.8 dominant wavelength (e). Differential seismogram for SMART layers with 1.8 dominant wavelength (f). The scale of the differential seismograms is two orders lower than the scale used to present the reference seismogram.

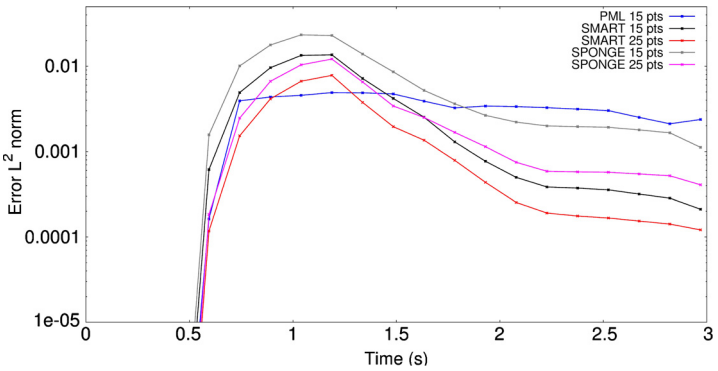

Fig. 2. Comparison of the evolution in time of the L^2 norm of the differential wavefields associated with the PML method with 1.1 dominant wavelength, the sponge layer method with 1.1 and 1.8 dominant wavelength, and the SMART layer method with 1.1 and 1.8 dominant wavelength.

We compare the seismograms obtained using PML, sponge layers, and SMART layers with the reference solution. For the PML method, the width of the layer is set to 150 m, which corresponds to 1.1 dominant wavelength (15 discretization points). For sponge and SMART layers, two simulations are performed: one with a 150 m width layer (1.1 dominant wavelength), the other with a 250 m width layer (1.8 dominant wavelength, or equivalently 25 discretization points).

The results are presented in Fig. 1. As expected, the PML are more accurate than sponge and SMART layers. This is illustrated by the differential seismograms obtained with the three methods. For the same layer width (150 m) (Figs. 1(b) to 1(d)), the amplitude of the PML residuals is smaller. The SMART layer method also provides a significant improvement with respect to sponge layers. In addition, we see that increasing the layer from 150 m to 250 m is sufficient for the SMART layer to yield differential seismogram comparable with the one yielded by the PML method. This is not true for the sponge layer method, which generates stronger amplitude residuals, even for a wider layer.

This qualitative analysis is complemented by a quantitative comparison of the L^2 norm of the error in the domain of interest at different times (Fig. 2). The error peak is attained at around $t = 1$ s, which corresponds to the time at which the wavefront reaches the layer. The weakest error is provided by the PML, while the largest is provided by the sponge layers. We see that using SMART layers significantly decreases the error compared to sponge layers. When the layer size is increased, the SMART layers error reaches the level of the PML error.

From this first comparison, we conclude that when no amplification occurs, the PML method is the more accurate. The Perfectly Matched property of the layer at the continuous level yields a very small reflection coefficient after discretization. The reflection coefficient of the SMART layer method is also clearly smaller than the one associated with the sponge layer method. In this sense, the SMART layer method is an improvement of the sponge layer technique.

The comparison of the three methods in terms of computational cost is difficult. The sponge and SMART layer do no require to split the unknowns as in the standard Bérenger formulation [9,25] or its M-PML variant [37,18], or the use of memory variables as in the CPML method [30]. The zero-order term associated with the sponge layer is diagonal, while the one associated with SMART layer may be full, depending on the wave propagation system considered (it is full for 2D acoustic TTI equations). Therefore, for a given layer size, one can expect the sponge layer to be the less expensive in terms of computational cost, followed by SMART layers and finally PML. However, as illustrated in Figs. 1 and 2, for reaching the same accuracy, the SMART layers and sponge layer sizes have to be multiplied respectively by 2 and 4. This increase

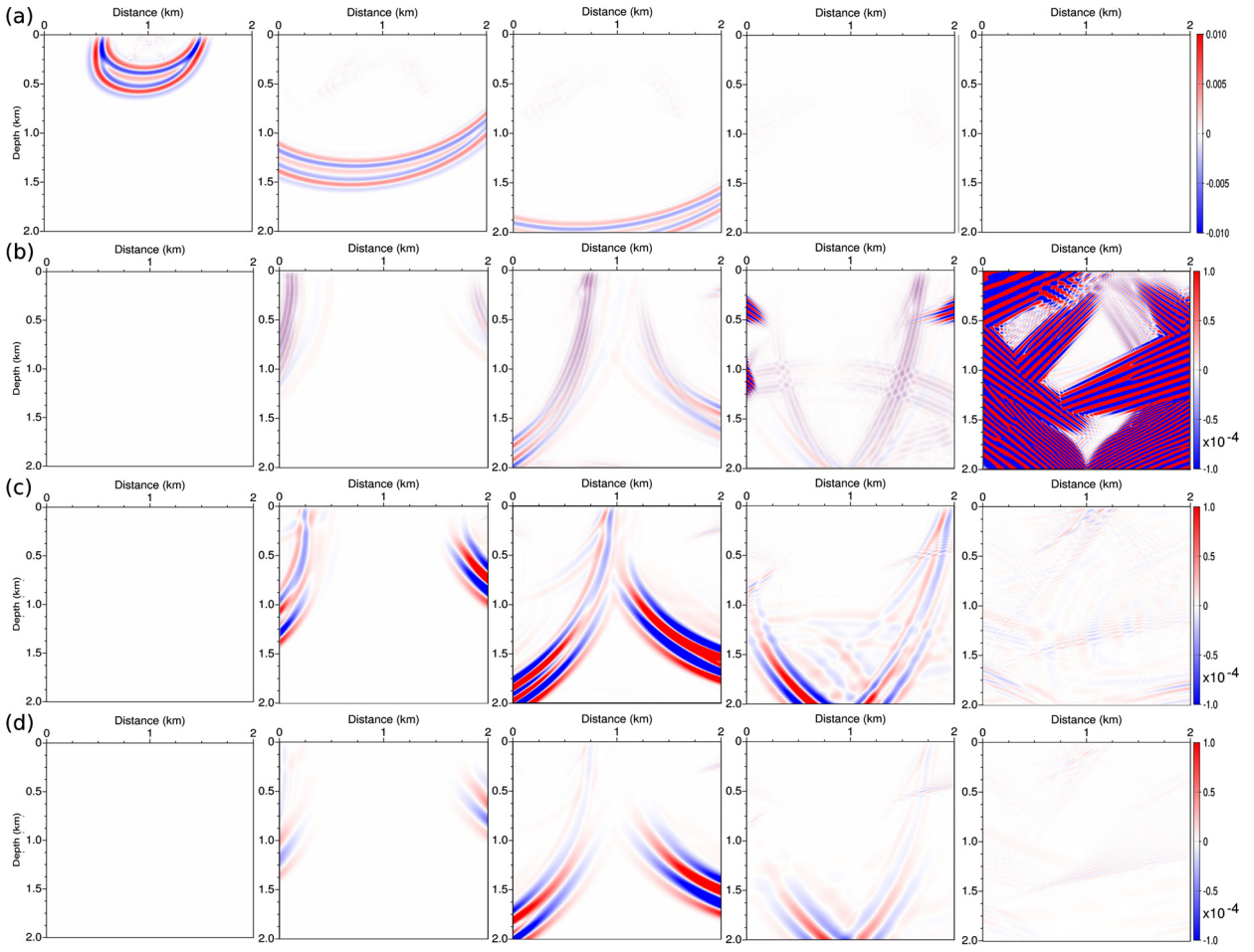

Fig. 3. Snapshots of the pressure wavefield $(\sigma_{xx}^{\theta} + \sigma_{zz}^{\theta})/2$ at times 0.3 s, 0.75 s, 1.15 s, 1.5 s, 3 s. Reference wavefields are computed in a large domain to ensure no reflection at the boundaries (row (a)). We compare the differential wavefield obtained using the PML method with 1.1 dominant wavelength (row (b)), the SMART layer method with 1.1 dominant wavelength (row (c)), the SMART layer method with 1.8 dominant wavelength (row (d)). The scale of the residuals wavefields is two orders lower than the scale used to present the reference wavefields.

seems difficult to be compensated only by the reduction of the number of operations, especially in 3D cases. This qualitative analysis supports the idea that when PML becomes amplifying (as illustrated in the next experiment), SMART layers should be used instead of sponge layers, as thinner layers can be used.

4.3. Robustness comparison between PML and SMART layers

We now consider a medium with anelliptical anisotropy

- $v_P = 2000\ \mathrm{m\,s^{-1}}$, $\rho = 1000\ \mathrm{kg\,m^{-3}}$,
- $\epsilon = 0.3 > \delta = 0.1$ (anelliptical case),
- $\theta = 36°$.

We keep the same configuration as for the previous experiment. We compute a reference solution in an extended domain, sufficiently large to ensure no reflections at its boundaries during the simulation length. Reference wavefields are stored at the recording times

- $t_1 = 0.3$ s, $t_2 = 0.75$ s, $t_3 = 1.15$ s, $t_4 = 1.5$ s, $t_5 = 3$ s

We present the residuals wavefields for each simulation, at each time t_i in Fig. 3. The residuals wavefields are simply calculated by difference between the layer methods solution and the reference wavefield at a given time in the domain of interest. We also present the reference seismogram and the differential seismograms obtained with PML and SMART layers in Fig. 4.

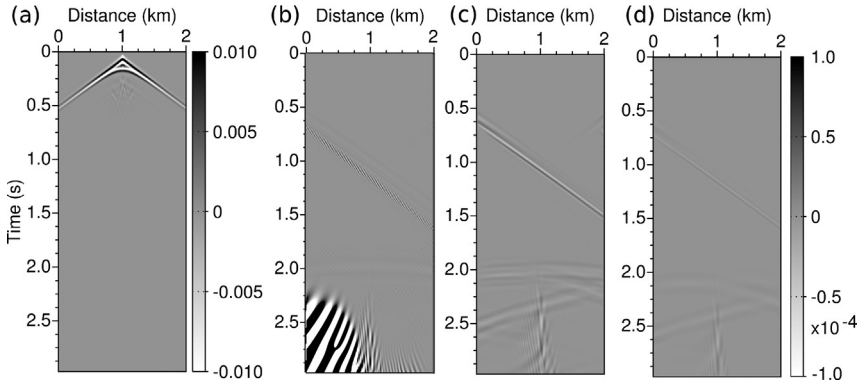

Fig. 4. Anelliptical case ($\epsilon > \delta$). Reference seismogram (a). Differential seismogram for PML layers with 1.1 dominant wavelength (b), for SMART layers with 1.1 dominant wavelength (c), for SMART layers with 1.8 dominant wavelength (d). The scale of the differential seismograms is two orders lower than the scale used to present the reference seismogram.

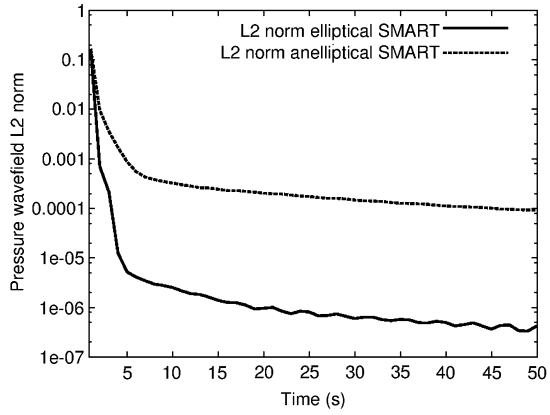

Fig. 5. History of the L^2 norm of the pressure wavefield in the domain of interest using the SMART strategy with a 1.1 dominant wavelength width layer for a long time simulation (50 s).

As already reported in previous studies [7,38,19,47], the PML method yields exponential amplification. This is emphasized by the differential wavefield snapshots at time $t = 1.5$ s and $t = 3$ s in Fig. 3(b), as well as in the differential seismograms presented in Fig. 4(b). This amplification becomes visible at a rather short simulation time ($t = 1.5$ s) and is not related with long-term amplification reported for instance for Maxwell's equations [1]. In this latter case, the amplification may be due to numerical inaccuracy of the discrete implementation, while the amplification is here intrinsically associated with the continuous form of the PML equations for acoustic TI anisotropy. Conversely, the SMART layer remains dissipative, which confirms the analysis provided in the previous sections.

To complete this study, and ensure that the SMART layers are robustly dissipative, we perform an additional simulation. We set the total simulation time to $t = 50$ s and compute the L^2 norm history of the pressure wavefield using the SMART method with a 1.1 dominant wavelength width layer. The results are presented in Fig. 5. The L^2 norm of the pressure wavefield decreases in both cases down to values close to 10^{-7} for the elliptical case and 10^{-5} for the general case. The presence of S-waves in the latter case seems to generate numerical noise whose amplitude decreases more slowly compared to the elliptical case. However, the level of the remaining signal after 50 s of simulation is several order of magnitudes lower than the initial wavefront in both cases.

These experiments thus confirm numerically that the SMART layer method is dissipative, even for long-time simulations, in anelliptical anisotropic media.

4.4. Efficient S-wave filter at the source

Besides the robust dissipation provided by the SMART layer, the method presents an another interesting feature, which is related to the selective damping strategy. It is indeed possible to distinguish between the wavefront associated with different wave velocities, these wave velocities corresponding to the eigenvalues of the matrices A_j. It is therefore possible to apply particular treatments to P-waves and S-waves as they are associated with different propagation speeds. The S-waves which are generated are considered as artifacts, and efficiently remove the imprint of these waves in the computed

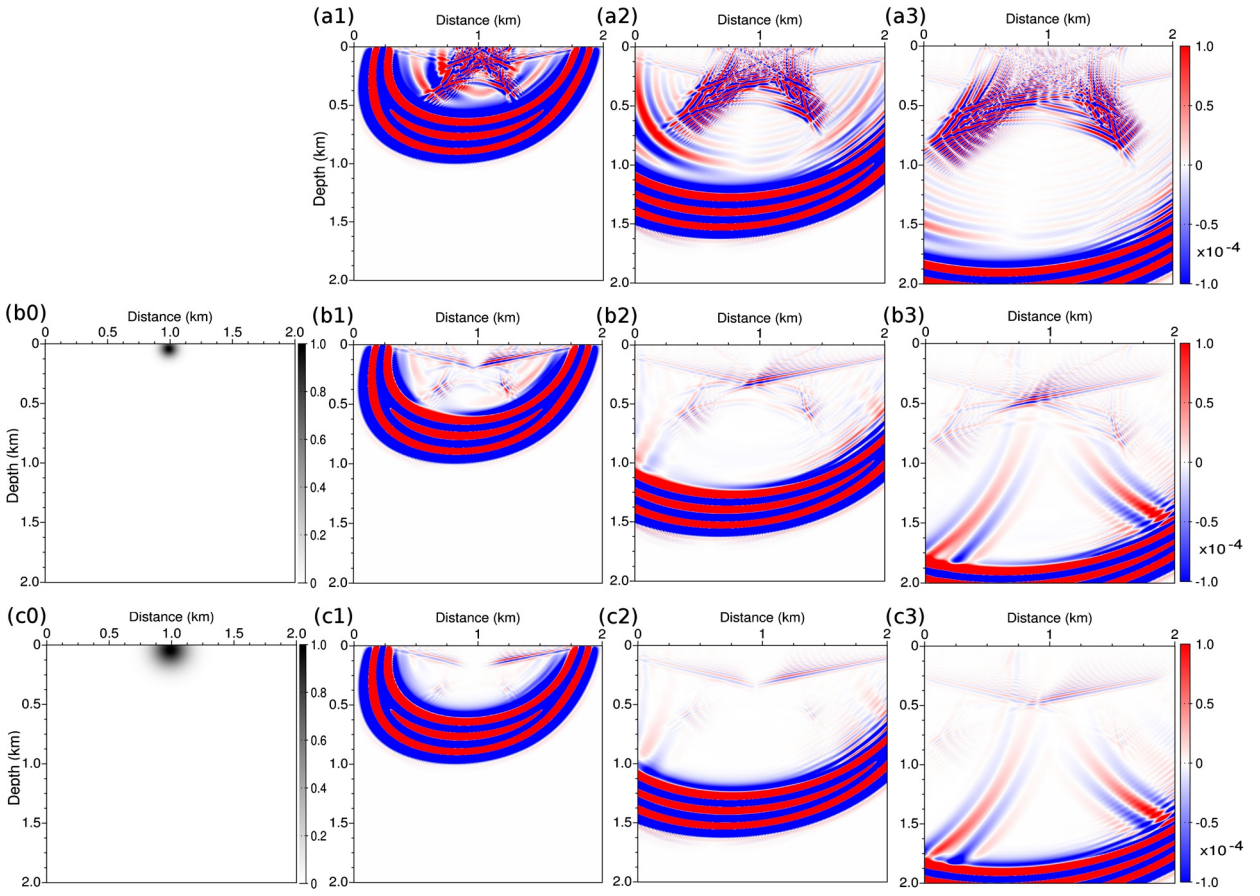

Fig. 6. Snapshots of the pressure wavefield $(\sigma_{xx}^{\theta}+\sigma_{zz}^{\theta})/2$ at $t=0.45$ s, $t=0.75$ s, $t=1.15$ s, in the general case $\epsilon>\delta$. Reference wavefields are computed in a large domain to ensure no reflection at the boundaries (row (a)). We compare the reference wavefields with the wavefield obtained using the SMART layer method with 25 grid points with a damping of S-waves imposed in a Gaussian zone around the source, with a characteristic length σ equal to 50 m (row (b)), and 100 m (row (c)). The damping zones are presented to the left (panels b_0 and c_0). The amplitude of S-waves, clearly visible in the reference wavefields, is strongly decreased in the two SMART layer simulations.

wavefield remains a challenge. In practice, the source implementation we use already strongly reduces the amplitude of the S-waves [38]. It is also possible to define an artificial zone around the source in which the media is forced to be elliptical to prevent the generation of S-waves, as proposed by Duveneck et al. [20]. However, both strategies are not fully satisfactory: in the first case, non-negligible S-waves still propagate in the computational domain, as can be seen in Fig. 3. In the second case, imposing the medium to be elliptical around the source may impact the accuracy of the simulations and generate artificial reflections at the interface between the artificial elliptical zone and the domain of interest.

The selective damping strategy on which relies the SMART layer seems to provide a more natural remedy to this problem. As the method offers the possibility to damp S-waves or P-waves, an efficient way of reducing the generation of S-waves is to define a small zone around the source in which a strong S-wave damping is imposed. This is similar to the second strategy, with the advantage of not requiring to impose an artificial locally elliptical anisotropy. We thus perform the following numerical experiment to illustrate the potential of the SMART layer. We keep the source implementation used in the previous experiments [38]. A Gaussian function $\mathcal{D}(x,z)$ defines the damping zone around the source

$$\mathcal{D}(x,z)=e^{\frac{(x-x_S)^2}{2\sigma^2}}e^{\frac{(z-z_S)^2}{2\sigma^2}} \tag{118}$$

The zero-order term $B(x,z)$ added by the SMART layer method is modified into $B_{\mathcal{D}}(x,z)$ such that

$$B_{\mathcal{D}}(x,z)=B(x,z)+\mathcal{D}(x,z)\sum_{j=1}^{2}\left(B_{jS}^{+}(x,z)+B_{jS}^{-}(x,z)\right) \tag{119}$$

We perform two simulations: one for $\sigma=50$ m, the other for $\sigma=100$ m. We compare the wavefields in the domain of interest at times $t=0.45$ s, $t=0.75$ s, $t=1.15$ s with a reference wavefield computed in a domain large enough to ensure no reflection at its boundaries. The results are presented in Fig. 6. The color scale for the representation of all the wavefields

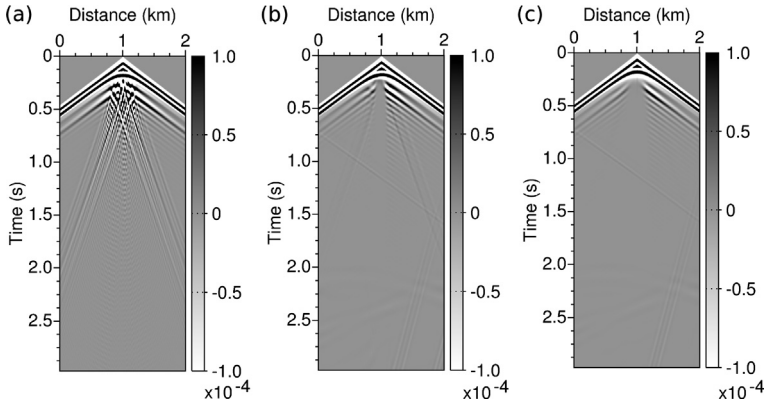

Fig. 7. Reference seismogram (a). Seismograms computed using a 1.8 dominant wavelength width SMART layer with a damping of S-waves imposed in a Gaussian zone around the source, with a characteristic length σ equal to 50 m (b), and 100 m (c) an S-waves. The imprint of S-waves is strongly decreased in the case (b) and almost vanishes in the case (c).

is the one chosen to plot the differential wavefield in Fig. 3 so as to emphasize the presence of the S-waves. The results presented in Fig. 6 clearly demonstrate that these artifacts are efficiently reduced, even using a small damping zone (b). Enlarging the damping zone around the source removes almost completely the spurious S-waves (c).

This result is confirmed by the analysis of the seismograms presented in Fig. 7. Again, the scale chosen is the one corresponding to the differential seismograms of Figs. 1 and 4 to highlight the presence of S-waves, propagating at a lower speed than P-waves. The amplitude of these S-waves is strongly reduced in the seismogram associated with the SMART layer simulation using a small damping zone (b), and disappear almost completely using a larger damping zone (c).

5. Conclusion and perspectives

The SMART layer method seems to be a reliable alternative to the PML method for simulating wave propagation in anisotropic media. Applying the SMART layer implies the addition of a zero-order term to the initial hyperbolic system which is shown to be dissipative as soon as the hyperbolic is symmetrizable. We show that the elastic VTI equations satisfy these assumptions, as well as the acoustic VTI and TTI derived systems. The symmetrizers for these equations are naturally derived using the compliance tensor, which is the inverse of the stiffness tensor.

Numerical experiments on a homogeneous domain emphasize the robustness of the SMART layers compared to the PML. While the PML are amplifying in the general case $\epsilon > \delta$, the SMART layers are dissipative, even for long-time simulations (50 s).

The SMART layers are, as expected, less accurate than the PML method, as they are not perfectly matched: the reflection coefficient at the interface between the domain of interest and the computational domain is non-zero for waves arriving at non-normal incidence. However, compared to the sponge layer strategy, which is also unconditionally dissipative, the SMART layer method is shown to be more accurate, allowing to use thinner layers.

Besides these properties, the selective damping strategy on which relies the SMART layer also allows to implement an efficient S-waves filter around the source to decrease the imprint of spurious S-waves in the general case. Two simulations performed with a Gaussian damping zone with characteristic length equal to 50 m and 100 m emphasize the efficiency of this strategy. This property may be of particular interest for seismic migration algorithms.

From the work presented in this study, several directions of investigation should be explored. First, the possibility of improving the accuracy of SMART layers should be studied. This could be done through extrapolation techniques, as proposed by Halpern et al. [25] under the name of Harmoniously Matched Layers. Another possibility consists in designing fractal layers in order to break the coherence of the reflected signal at the interface between the domain of interest and the layer. The use of absorbing boundary condition more accurate than standard first-order radiation boundary condition at the external boundary could also be investigated, as it should allow to use lower absorption coefficients, and therefore reduce the reflections.

A second step of this work includes the application of the method to a realistic benchmark model for seismic wave propagation. We propose preliminary results on the BP2007 model in [35,36], and further studies should be led.

The SMART layer method can also be used to overcome long time instabilities observed for elasto-dynamic or Maxwell's equations in isotropic media. In these applications, the numerical discretization of the PML equations is responsible for the appearance of amplified waves after long simulation time. In [41], this type of instability is exhibited for 2D elasto-dynamic equations discretized with a Discontinuous Galerkin Finite Element method. The SMART layer is shown to be an efficient remedy to this instability.

Future studies will be done toward the application of the SMART layer method to 3D elasto-dynamic equation with triclinic anisotropy. Ultimately, the interest of the method should be tested within FWI and RTM algorithms for seismic imaging application in anisotropic media.

Acknowledgements

This study was partially funded by the SEISCOPE II consortium (http://seiscope2.osug.fr), sponsored by BP, CGG, Chevron, EXXON-MOBIL, JGI, Petrobras, SAUDI ARAMCO, Shell, SINOPEC, STATOIL, TOTAL and WESTERNGECO. This study was granted access to the HPC facilities of CIMENT (Université Joseph Fourier, Grenoble). Many thanks are due to Laurence Halpern and Jeffrey Rauch for their advice and inspiring comments.

References

[1] S. Abarbanel, D. Gottlieb, J.S. Hesthaven, Long-time behavior of the perfectly matched layer equations in computational electromagnetics, J. Sci. Comput. 17 (2002) 405–422.
[2] S. Abarbanel, D. Gottlieb, J.S. Hesthaven, Well-posed perfectly matched layers for advective acoustics, J. Comput. Phys. 154 (2) (1999) 266–283.
[3] T. Alkhalifah, Acoustic approximations for processing in transversely isotropic media, Geophysics 63 (1998) 623–631.
[4] T. Alkhalifah, An acoustic wave equation for anisotropic media, Geophysics 65 (2000) 1239–1250.
[5] D. Appelö, G. Kreiss, A new absorbing layer for elastic waves, J. Comput. Phys. 215 (2) (2006) 642–660.
[6] U. Basu, A.K. Chopra, Perfectly matched layers for time-harmonic elastodynamics of unbounded domains: theory and finite-element implementation, Comput. Methods Appl. Mech. Eng. 192 (2003) 1337–1375.
[7] E. Becache, S. Fauqueux, P. Joly, Stability of perfectly matched layers, group velocities and anisotropic waves, J. Comput. Phys. 188 (2003) 399–433.
[8] E. Becache, D. Givoli, T. Hagstrom, High-order absorbing boundary conditions for anisotropic and convective wave equations, J. Comput. Phys. 229 (2010) 1099–1129.
[9] J.-P. Bérenger, A perfectly matched layer for absorption of electromagnetic waves, J. Comput. Phys. 114 (1994) 185–200.
[10] J.P. Bérenger, Three-dimensional perfectly matched layer for the absorption of electromagnetic waves, J. Comput. Phys. 127 (2) (1996) 363–379.
[11] A. Bermúdez, L. Hervella-Nieto, A. Prieto, R. Rodríguez, An optimal perfectly matched layer with unbounded absorbing function for time-harmonic acoustic scattering problems, J. Comput. Phys. 223 (2) (2007) 469–488.
[12] R. Burridge, Elastic waves in anisotropic media, Schlumberger-Doll Research, 1996.
[13] C. Cerjan, D. Kosloff, R. Kosloff, M. Reshef, A nonreflecting boundary condition for discrete acoustic and elastic wave equations, Geophysics 50 (4) (1985) 2117–2131.
[14] R. Clayton, B. Engquist, Absorbing boundary conditions for acoustic and elastic wave equations, Bull. Seismol. Soc. Am. 67 (1977) 1529–1540.
[15] F. Collino, High order absorbing boundary conditions for wave propagation models: straight line boundary and corner cases, in: Proceedings of the Second International Conference on Mathematical and Numerical Aspects of Wave Propagation, SIAM, Delaware, 1993, pp. 161–171.
[16] F. Collino, C. Tsogka, Application of the perfectly matched absorbing layer model to the linear elastodynamic problem in anisotropic heterogeneous media, Geophysics 66 (2001) 294–307.
[17] J. Diaz, P. Joly, A time domain analysis of PML models in acoustics, Comput. Methods Appl. Mech. Eng. 195 (29–32) (2006) 3820–3853.
[18] M.M. Dmitriev, V.V. Lisitsa, Application of M-PML reflectionless boundary conditions to the numerical simulation of wave propagation in anisotropic media. Part I: reflectivity, Numer. Anal. Appl. 4 (4) (2011) 271–280.
[19] E. Duveneck, P.M. Bakker, Stable P-wave modeling for reverse-time migration in tilted TI media, Geophysics 76 (2) (2011) S65–S75.
[20] E. Duveneck, P. Milcik, P.M. Bakker, C. Perkins, Acoustic VTI wave equations and their application for anisotropic reverse-time migration, in: SEG Technical Program Expanded Abstracts, vol. 27 (1), 2008, pp. 2186–2190.
[21] B. Engquist, A. Majda, Absorbing boundary conditions of the numerical simulation of waves, Math. Comput. 31 (1977) 629–651.
[22] J. Etgen, S.H. Gray, Y. Zhang, An overview of depth imaging in exploration geophysics, Geophysics 74 (6) (2009) WCA5–WCA17.
[23] D. Givoli, High-order non-reflecting boundary conditions without high-order derivatives, J. Comput. Phys. 170 (2) (2001) 8.
[24] V. Grechka, L. Zhang, J.W. Rector III, Shear waves in acoustic anisotropic media, Geophysics 69 (2004) 576–582.
[25] L. Halpern, S. Petit-Bergez, J. Rauch, The analysis of matched layers, Confluent. Math. 3 (2) (2011) 159–236.
[26] F.D. Hastings, J.B. Schneider, S.L. Broschat, Application of the perfectly matched layer (PML) absorbing boundary condition to elastic wave propagation, J. Acoust. Soc. Am. 100 (1996) 3061–3069.
[27] J. Hesthaven, On the analysis and construction of perfectly matched layers for the linearized Euler equations, J. Comput. Phys. 142 (1998) 129–147.
[28] F.Q. Hu, On absorbing boundary conditions for linearized Euler equations by a perfectly matched layer, J. Comput. Phys. 129 (1) (1996) 201–219.
[29] M. Israeli, S.A. Orszag, Approximation of radiation boundary conditions, J. Comput. Phys. 41 (1981) 115–135.
[30] D. Komatitsch, R. Martin, An unsplit convolutional perfectly matched layer improved at grazing incidence for the seismic wave equation, Geophysics 72 (5) (2007) SM155–SM167.
[31] D. Komatitsch, J. Tromp, A perfectly matched layer absorbing boundary condition for the second-order seismic wave equation, Geophys. J. Int. 154 (1) (2003) 146–153.
[32] H.O. Kreiss, J. Lorenz, Initial–Boundary Value Problems and the Navier–Stokes Equations, Classics in Applied Mathematics, vol. 47, SIAM, 2004.
[33] R. Martin, D. Komatitsch, An unsplit convolutional perfectly matched layer technique improved at grazing incidence for the viscoelastic wave equation, Geophys. J. Int. 179 (2009) 333–344.
[34] R. Martin, D. Komatitsch, A. Ezziani, An unsplit convolutional perfectly matched layer improved at grazing incidence for seismic wave propagation in poroelastic media, Geophysics 73 (4) (2008) 51–61.
[35] L. Métivier, R. Brossier, S. Operto, J. Virieux, A robust absorbing layer method for seismic wave simulation in anisotropic media, in: Expanded Abstracts, 76th Annual EAGE Meeting, Amsterdam, 2014.
[36] L. Métivier, R. Brossier, S. Operto, J. Virieux, SMART: robust absorbing layer and S-waves filtering for acoustic anisotropic wave simulation, in: Expanded Abstracts, 84th Annual SEG Meeting, Denver, 2014.
[37] K.C. Meza-Fajardo, A.S. Papageorgiou, A nonconvolutional, split-field, perfectly matched layer for wave propagation in isotropic and anisotropic elastic media: stability analysis, Bull. Seismol. Soc. Am. 98 (4) (2008) 1811–1836.
[38] S. Operto, J. Virieux, A. Ribodetti, J.E. Anderson, Finite-difference frequency-domain modeling of visco-acoustic wave propagation in two-dimensional TTI media, Geophysics 74 (5) (2009) T75–T95.
[39] Q. Qi, T.L. Geers, Evaluation of the perfectly matched layer for computational acoustics, J. Comput. Phys. 139 (1) (1998) 166–183.
[40] E.H. Saenger, N. Gold, S.A. Shapiro, Modeling the propagation of elastic waves using a modified finite-difference grid, Wave Motion 31 (2000) 77–92.
[41] J. Tago, L. Métivier, J. Virieux, Smart layers: a simple and robust alternative to PML approaches for elastodynamics, Geophys. J. Int. 199 (2) (2014) 700–706, http://dx.doi.org/10.1093/gji/ggu298.
[42] L.A. Thomsen, Weak elastic anisotropy, Geophysics 51 (1986) 1954–1966.
[43] J. Virieux, P–SV wave propagation in heterogeneous media, velocity-stress finite difference method, Geophysics 51 (1986) 889–901.
[44] J. Virieux, S. Operto, An overview of full waveform inversion in exploration geophysics, Geophysics 74 (6) (2009) WCC1–WCC26.

[45] D. Yang, S. Wang, Z. Zhang, J. Teng, *n*-times absorbing boundary conditions for compact finite-difference modeling of acoustic and elastic wave propagation in the 2D TI medium, Bull. Seismol. Soc. Am. 93 (6) (2003) 2389–2401.
[46] K.S. Yee, Numerical solution of initial boundary value problems involving Maxwell's equations in isotropic media, IEEE Trans. Antennas Propag. 14 (1966) 302–307.
[47] Y. Zhang, H. Zhang, G. Zhang, A stable TTI reverse time migration and its implementation, Geophysics 76 (3) (2011) WA3–WA11.
[48] H. Zhou, G. Zhang, R. Bloor, An anisotropic acoustic wave equation for modeling and migration in 2D TTI media, in: Expanded Abstracts – New Orleans, vol. 25, Society of Exploration Geophysics, 2006, pp. 194–198.